

THE STRUCTURE OF A LOW-METALLICITY GIANT MOLECULAR CLOUD COMPLEX

ADAM K. LEROY¹, ALBERTO BOLATTO², CAROLINE BOT³, CHARLES W. ENGELBRACHT⁴, KARL GORDON⁵, FRANK P. ISRAEL⁶, MÓNICA RUBIO⁷, KARIN SANDSTROM⁸, AND SNEŽANA STANIMIROVIĆ⁹

Accepted for publication in The Astrophysical Journal

ABSTRACT

To understand the impact of low metallicities on giant molecular cloud (GMC) structure, we compare far infrared dust emission, CO emission, and dynamics in the star-forming complex N83 in the Wing of the Small Magellanic Cloud. Dust emission (measured by *Spitzer* as part of the S³MC and SAGE-SMC surveys) probes the total gas column independent of molecular line emission and traces shielding from photodissociating radiation. We calibrate a method to estimate the dust column using only the high-resolution *Spitzer* data and verify that dust traces the ISM in the H I-dominated region around N83. This allows us to resolve the relative structures of H₂, dust, and CO within a giant molecular cloud complex, one of the first times such a measurement has been made in a low-metallicity galaxy. Our results support the hypothesis that CO is photodissociated while H₂ self-shields in the outer parts of low-metallicity GMCs, so that dust/self shielding is the primary factor determining the distribution of CO emission. Four pieces of evidence support this view. First, the CO-to-H₂ conversion factor averaged over the whole cloud is very high $4\text{--}11 \times 10^{21} \text{ cm}^{-2} (\text{K km s}^{-1})^{-1}$, or 20–55 times the Galactic value. Second, the CO-to-H₂ conversion factor varies across the complex, with its lowest (most nearly Galactic) values near the CO peaks. Third, bright CO emission is largely confined to regions of relatively high line-of-sight extinction, $A_V \gtrsim 2$ mag, in agreement with PDR models and Galactic observations. Fourth, a simple model in which CO emerges from a smaller sphere nested inside a larger cloud can roughly relate the H₂ masses measured from CO kinematics and dust.

Subject headings: Galaxies: ISM — (galaxies:) Magellanic Clouds — infrared: galaxies — (ISM:) dust, extinction — ISM: clouds — stars: formation

1. INTRODUCTION

Most star formation takes place in giant molecular clouds (GMCs). A quantitative understanding of how local conditions affect the structure and evolution of these clouds is key to link conditions in the interstellar medium (ISM) to stellar output. Achieving such an understanding is unfortunately complicated by the fact that H₂ does not readily emit under the conditions inside a typical GMC. Astronomers therefore rely on indirect tracers of H₂, most commonly CO line emission and dust absorption or emission. These tracers are also affected by environment, so that assessing the impact of local conditions on GMC structure requires disentangling the effect of these conditions on the adopted tracer from their effect on the underlying distribution of H₂.

One way around this problem is to use several independent methods to measure the structure of GMCs in extreme environments, inferring the state of H₂ by

comparing the results. Here we apply this approach to an active star-forming region in the Small Magellanic Cloud (SMC). Using far infrared (FIR) emission measured by the *Spitzer* Survey of the SMC (S³MC Bolatto et al. 2007) and SAGE-SMC (“Surveying the Agents of a Galaxy’s Evolution in the SMC”, Gordon et al. in prep.), we derive the distribution of dust in the region. We compare this to maps of CO and H I line emission (Bolatto et al. 2003; Stanimirovic et al. 1999). Dust traces the total gas distribution — of which the atomic component is already known — and offers a probe of shielding from dissociating UV radiation. CO is the most common molecule after H₂ (and the most commonly used tracer of molecular gas); understanding its relation to H₂ in extreme environments is a long-standing goal. The CO line also carries kinematic information that allows dynamical estimates of cloud masses.

The SMC is of particular interest because the ISM in dwarf irregular galaxies like the SMC contrast sharply with that of the Milky Way. They have low metallicities (e.g., Lee et al. 2006), correspondingly low dust-to-gas ratios (e.g., Issa et al. 1990; Walter et al. 2007), and intense radiation fields (e.g., Madden et al. 2006). These factors should affect the formation and structure of GMCs (e.g., Maloney & Black 1988; Elmegreen 1989; McKee 1989; Papadopoulos et al. 2002; Pelupessy et al. 2006). Unfortunately, it has proved extremely challenging to unambiguously observe such effects because the inferred structure of GMCs depends sensitively on the method used to trace H₂.

Virial mass calculations reveal few differences between GMCs in dwarf galaxies and those in the Milky Way.

¹ Max-Planck-Institut für Astronomie, D-69117 Heidelberg, Germany

² Department of Astronomy, University of Maryland, College Park, MD 20742

³ UMR 7550, Observatoire Astronomiques de Strasbourg, Université Louis Pasteur, F-67000 Strasbourg, France

⁴ Steward Observatory, University of Arizona, Tucson, AZ 85721

⁵ Space Telescope Science Institute, 3700 San Martin Drive, Baltimore, MD 21218, USA

⁶ Sterrewacht Leiden, Leiden University, PO Box 9513, 2300 RA Leiden

⁷ Departamento de Astronomía, Universidad de Chile, Casilla 36-D

⁸ Department of Astronomy and Radio Astronomy Laboratory, University of California, Berkeley, CA 94720

⁹ Astronomy Department, University of Wisconsin, Madison, 475 N. Charter St., WI 53711, USA

In this approach, one uses molecular line emission to measure the size and line width of a GMC. By assuming a density profile and virial equilibrium, one can estimate the dynamical mass of the cloud independent of its luminosity. Recent studies find the ratio of virial mass to luminosity for GMCs in other galaxies to be very similar to that observed in the Milky Way (Walter et al. 2001, 2002; Rosolowsky et al. 2003; Bolatto et al. 2003; Israel et al. 2003; Leroy et al. 2006; Blitz et al. 2007; Bolatto et al. 2008). Further, the scaling relations among GMC size, line width, and luminosity found in the Milky Way (Larson 1981; Solomon et al. 1987; Heyer et al. 2008) seem to approximately apply to resolved CO emission in other galaxies, even dwarf galaxies (Bolatto et al. 2008).

By contrast, observations of low metallicity galaxies that do not depend on molecular line emission consistently suggest large reservoirs of H_2 untraced by CO (e.g., Israel 1997b; Madden et al. 1997; Pak et al. 1998; Boselli et al. 2002; Galliano et al. 2003; Rubio et al. 2004; Leroy et al. 2007; Bot et al. 2007). The most common manifestation of this is an “excess” at FIR or submillimeter wavelengths with the following sense: towards molecular peaks, there is more dust emission than one would expect given the gas column estimated from H I + CO. Israel (1997b) treated the abundance of H_2 as an unknown and used this excess to solve for the CO-to- H_2 conversion factor. He found it to depend strongly on both metallicity and radiation field.

These two sets of observations may be reconciled if CO is selectively photodissociated in the outer parts of low-metallicity GMCs (e.g. Maloney & Black 1988; Israel 1988; Bolatto et al. 1999), a scenario discussed specifically for the SMC by Israel et al. (1986) and Rubio et al. (1991, 1993a). This might be expected if H_2 readily self-shields while CO is shielded from photodissociating radiation mostly by dust, which is less abundant at low metallicities. In this case, CO emission would trace only the inner parts of low-metallicity GMCs.

Observations of the Magellanic Clouds as part of the Swedish-ESO Submillimeter Telescope (SEST) Key Programme (Israel et al. 1993) support this idea: the surface brightness of CO is very low in the SMC (Rubio et al. 1991); SMC clouds tend to be smaller than their Milky Way counterparts, with little associated diffuse emission (Rubio et al. 1993a; Israel et al. 2003); and the ratio of ^{13}CO to ^{12}CO emission is lower in the Magellanic Clouds than in the Galaxy, suggesting that clouds are more nearly optically thin (Israel et al. 2003).

The SEST results are mainly indirect evidence. What is still needed is a direct, *resolved* comparison between CO, dust, and H_2 . Because dust emission offers a tracer of the total gas distribution that is independent of molecular line emission (Thronson et al. 1987, 1988; Thronson 1988; Israel 1997b), it allows such a test. If GMCs at low metallicity include envelopes of CO-free H_2 , then the distribution of dust (after subtracting the dust associated with H I) should be extended relative to CO emission.

Leroy et al. (2007) attempted this measurement. They combined S³MC with IRIS data (Miville-Deschénes & Lagache 2005) to derive the distribution of dust and compared this to the NANTEX CO survey by Mizuno et al. (2001). They derived a

distribution of $H_2 \sim 1.3$ times more extended than that of CO, suggesting that half of the H_2 in the SMC may lie in envelopes surrounding the CO peaks. The resolution of the CO and IRIS data limited this comparison to scales of $\gtrsim 45$ pc. SMC GMCs are often much smaller than this (e.g. Rubio et al. 1993a; Mizuno et al. 2001; Israel et al. 2003). Therefore while this measurement indicated that SMC GMC complexes may be immersed in a sea of CO-free cold gas, it was not yet a true comparison of dust and CO on the scales of individual GMCs.

Here, we focus on a single region, N83/N84 (hereafter simply N83). This isolated star-forming complex lies in the eastern Wing of the SMC and harbors $\sim 10\%$ of that galaxy’s total CO luminosity (Mizuno et al. 2001). Combining FIR, CO, and H I data we attempt to answer following questions:

1. What is the CO-to- H_2 conversion factor, X_{CO} (i.e., the ratio of H_2 column density to CO intensity along a line of sight) in this region?
2. Is there evidence that CO is less abundant relative to H_2 (i.e., that X_{CO} is higher or that there is H_2 without associated CO) in the outer parts of the cloud?
3. Is the distribution of CO consistent with dust shielding playing a key role in its survival?
4. Can dynamical masses measured from CO kinematics be brought into agreement with H_2 masses estimated from dust? What is the implied distribution of H_2 ?

To meet these goals, we first estimate the dust optical depth at $160\mu\text{m}$, τ_{160} (§3). We demonstrate that τ_{160} traces H I column density in the (assumed) H I-dominated ISM near N83, make a self-consistent determination of the dust-to-gas ratio, and then combine τ_{160} with the measured H I column density to estimate the H_2 column density in the star forming region (§4). Finally, we combine the resulting maps of τ_{160} and H_2 with CO and H I data to answer the questions posed above (§5).

2. DATA

We use FIR imaging from two *Spitzer* surveys. S³MC mapped 70 and $160\mu\text{m}$ emission from most active star forming regions in the SMC, including N 83. More recently, SAGE-SMC observed a much larger area, including the Magellanic Bridge and nearby emission-free regions. We use a combination of these data sets carried out by Gordon et al. (in prep.) that dramatically improves the quality of the $70\mu\text{m}$ image compared to S³MC alone, thus enabling this analysis. At $36''$ resolution, the noise (1σ) in the *Spitzer* maps is $\sigma_{70} = 0.13 \text{ MJy ster}^{-1}$ ($70\mu\text{m}$) and $\sigma_{160} = 0.6 \text{ MJy ster}^{-1}$ ($160\mu\text{m}$) in the neighborhood of N83.

We compare the *Spitzer* data to the IRIS $100\mu\text{m}$ image. IRIS is a re-processing of the IRAS data carried out by Miville-Deschénes & Lagache (2005). These data have $\sim 4.3'$ resolution.

Bolatto et al. (2003) used SEST to map CO $J = 2 \rightarrow 1$ and $J = 1 \rightarrow 0$ emission from N83. The half-power beam width of SEST was $23''$ ($J = 2 \rightarrow 1$) and $45''$

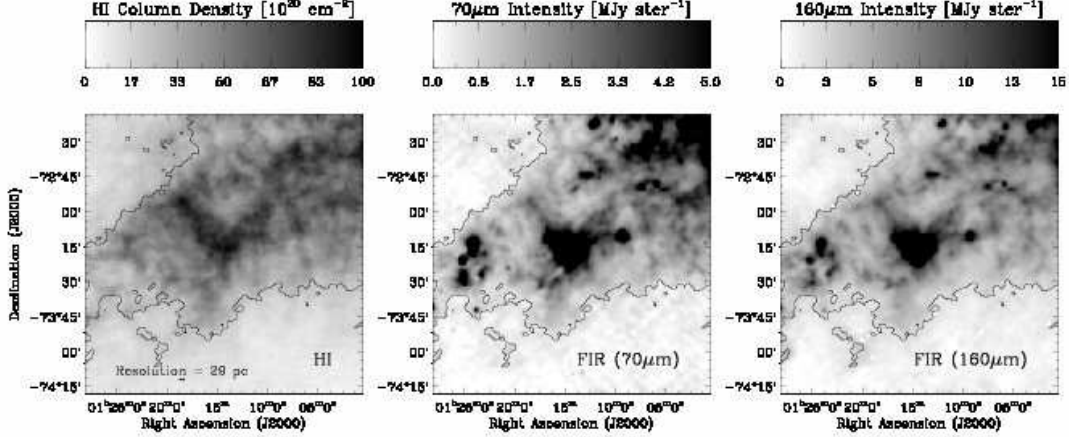


FIG. 1.— H I (left) and FIR emission at 70 (middle) and 160 μm (right) in a two degree wide field centered on N 83. A thin black contour outlines the region where we can clearly distinguish FIR emission from the background (see §2.1).

($J = 1 \rightarrow 0$). The maps that we use were convolved to lower resolution during reduction and have final angular resolutions of 38'' ($J = 2 \rightarrow 1$) and 55'' ($J = 1 \rightarrow 0$). The noise in the velocity-integrated maps is somewhat position-dependent. Over regions with significant emission 1σ is typically 0.16 K km s $^{-1}$ (CO $J = 2 \rightarrow 1$) and 0.22 K km s $^{-1}$ (CO $J = 1 \rightarrow 0$).

Stanimirovic et al. (1999) imaged H I 21-cm line emission across the whole SMC. These data have angular resolution 98'' and sensitivity sufficient to detect H I emission along every line of sight within $\sim 1^\circ$ of N83. We correct for H I optical depth and self-absorption following Stanimirovic et al. (1999, their Equation 6) based on the H I absorption study by Dickey et al. (2000). The maximum correction factor near N83 is ~ 1.3 .

To subtract emission associated with the Milky Way from the FIR maps (§2.1), we use the Parkes map of Milky Way H I from Brüns et al. (2005). Galactic H I is distinguished from SMC gas by its radial velocity. These data have a resolution of 14'.

We move all data to three astrometric grids: one covering the entire SMC, a two degree wide field surrounding N 83 (Figure 1), and the SEST field. In the SEST field, we use the kernels of Gordon et al. (2008b) to place the 70 μm image at the 160 μm resolution ($\sim 36''$), which matches that of the SEST CO $J = 2 \rightarrow 1$ data (38'') well. We also convolve the 70 and 160 μm maps to the 55'' resolution of the SEST CO $J = 1 \rightarrow 0$ data. In the two degree field near N83, we use a Gaussian kernel to place the 70 and 160 μm data at the 98'' resolution of the H I. Over the whole SMC, we degrade the 70 and 160 μm images to the 4.3' IRIS resolution.

2.1. Additional Processing of the FIR Maps

For consistency among the 70, 100, and 160 μm data, we move flux densities at 70 and 160 μm from the MIPS scale (which assumes $F_\nu \propto \nu^2$ across the bandpass) to the IRAS scale (which assumes $F_\nu \propto \nu^{-1}$). We do so by dividing the 70 map by 0.918 and the 160 μm map by 0.959.

We subtract Milky Way foreground emission from the 100 and 160 μm maps. We estimate this from Galactic H I assuming the average cirrus dust properties measured by (Boulanger et al. 1996). At 100 μm we use their fit di-

rectly; at 160 μm we interpolate their fits assuming a typical cirrus dust temperature ($T = 17.5$ K) and emissivity ($\beta = 2$).

To refine the foreground subtraction, we assume that H I and infrared intensity from the SMC are correlated at a basic level. As the column density of SMC H I approaches 0, we expect the IR intensity of the SMC to also approach 0. Therefore, we adjust the zero point of the IR maps using a fit of IR intensity to $N(\text{H I})_{\text{SMC}}$ where $N(\text{H I})_{\text{SMC}} < 2 \times 10^{21} \text{ cm}^{-2}$ (we subtract the fitted y -intercept). This leads us to add 0.3 MJy ster $^{-1}$ at 70 μm , subtract 4.4 MJy ster $^{-1}$ at 160 μm , and subtract 0.5 MJy ster $^{-1}$ from the IRIS 100 μm map. These offsets are a natural consequence of the uncertainty in the reduction and foreground subtraction (which must remove zodiacal light, Milky Way cirrus, and any cosmic infrared background). Deviations from the average cirrus properties are particularly common, being observed near a number of galaxies by Bot et al. (2009).

Based on carrying out this exercise in several different ways, we estimate the zero level of our maps to be uncertain by 0.25 MJy ster $^{-1}$ at 70 μm and 1 MJy ster $^{-1}$ at 160 μm . We take these uncertainties into account in our calculations (§3.2). To minimize their impact we only consider lines of sight with intensities well above the background, by which we mean $I_{70} > 0.5 \text{ MJy ster}^{-1}$ and $I_{160} > 2 \text{ MJy ster}^{-1}$ after the foreground subtraction (i.e., twice the uncertainty in the background).

2.2. A Word on Resolution

In the rest of this paper we will combine the data described above in several ways. Two of these combinations lead to maps combining data with different resolutions. We comment on these here and the reader may wish to refer back to this section while reading the paper.

First, we subtract a foreground component measured at 14' resolution from IR maps with 4.3' and $\sim 36''$ (160 μm) resolution. Any small scale variation in the Milky Way cirrus will therefore be left in our maps. This is only a concern in the diffuse region of the Wing (and so only in §4.1). In N83 itself most lines of sight exhibit FIR intensities $\gtrsim 10$ times higher than the foreground, so variations in the foreground are not a concern.

Second, when estimating the distribution of H₂ in N83,

we derive the total amount of hydrogen ($\mathrm{H}\,\mathrm{I} + \mathrm{H}_2$) along a line of sight and then subtract the measured $\mathrm{H}\,\mathrm{I}$ column density. The total amount of hydrogen is based on FIR dust emission, measured at $36''$ resolution (or $55''$ resolution when we compare to the SEST CO $J = 1 \rightarrow 0$ map). The $\mathrm{H}\,\mathrm{I}$ column density is measured at $98''$ resolution. We assume it to be smooth on smaller scales, an assumption born out to some degree by the reasonable correlation that we find between H_2 and CO. Nonetheless, the detailed distribution of H_2 on scales less than $98''$ (~ 29 pc) is somewhat uncertain.

3. DUST TREATMENT

We use the optical depth at $160\mu\mathrm{m}$, τ_{160} , as a proxy for the amount of dust along a line of sight. For an optically thin population of grains with an equilibrium temperature T_{dust} , τ_{160} is related to the measured $160\mu\mathrm{m}$ intensity, I_{160} , by

$$\tau_{160} = \frac{I_{160}}{B_{\nu}(T_{\mathrm{dust}}, 160\mu\mathrm{m})}. \quad (1)$$

Here $B_{\nu}(T_{\mathrm{dust}}, \lambda)$ is the intensity of a blackbody of temperature T_{dust} at wavelength λ .

Calculating τ_{160} thus requires estimating T_{dust} . Because only the 70 and $160\mu\mathrm{m}$ maps have angular resolution appropriate to compare with CO, we must do so using this combination. Unfortunately, I_{70}/I_{160} does not trivially map to T_{dust} because the $70\mu\mathrm{m}$ band includes non-equilibrium emission from small grains (e.g., Desert et al. 1990; Draine & Li 2007; Bernard et al. 2008). We therefore take an indirect approach: we assume that most of the dust mass resides in large grains with equilibrium temperature T_{dust} that contribute all of the emission at $100\mu\mathrm{m}$ and $160\mu\mathrm{m}$. We use I_{70}/I_{160} to estimate I_{100}/I_{160} and then solve for T_{dust} from

$$\frac{I_{100}}{I_{160}} = \left(\frac{100}{160}\right)^{-1.5} \frac{B_{\nu}(T_{\mathrm{dust}}, 100\mu\mathrm{m})}{B_{\nu}(T_{\mathrm{dust}}, 160\mu\mathrm{m})}, \quad (2)$$

which assumes that dust has a wavelength-dependent emissivity such that $\tau_{\lambda} \propto \lambda^{-\beta}$ with $\beta = 1.5$.

We derive the relationship between I_{70}/I_{160} and I_{100}/I_{160} at the $4.3'$ resolution of IRIS, where both colors are known and exhibit a roughly 1-to-1 relation. We then assume this relationship to apply to the smaller ($\sim 36''$) angular scales measured only by the *Spitzer* data. Near N83, the two colors are related by:

$$\frac{I_{100}}{I_{160}} = 0.24x^2 + 0.33x + 0.45, \text{ where } x = \frac{I_{70}}{I_{160}}. \quad (3)$$

Note that this is not a general relation. It does not go through the origin and is only 1-to-1 over a limited range of I_{70}/I_{160} ; we fit and apply over the range $I_{70}/I_{160} \sim 0.15 - 1.2$, where it is a good description of the SMC.

3.1. Motivation

In assuming that I_{100}/I_{160} traces T_{dust} or its more sophisticated analogs (e.g., Dale & Helou 2002; Draine & Li 2007), we follow several recent studies of the Magellanic Clouds (Bot et al. 2004; Leroy et al. 2007; Bernard et al. 2008; Gordon et al. 2008a). Schnee et al. (2005, 2006, 2008) have demonstrated that a similar

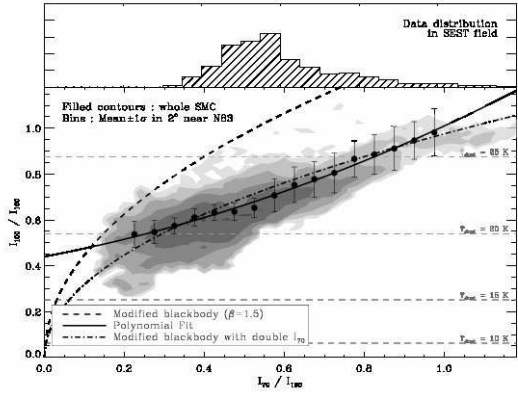


FIG. 2.— FIR color-color plot for the SMC. The x -axis shows I_{70}/I_{160} , which is measured by *Spitzer* at high resolution but includes contamination by non-equilibrium emission. The y -axis shows I_{100}/I_{160} , which is only available at $4.3'$ resolution but is more likely to trace exclusively equilibrium emission. Horizontal dashed lines show the temperatures associated with a few values of this color. Shaded contours show the distribution of data for the whole SMC; the lowest contour includes all data and the contour increment is a factor of 4 in data density. Black circles show mean and 1σ scatter for data in a 2° field centered on N83 (binned by I_{70}/I_{160}). The histogram above the plot shows the distribution of I_{70}/I_{160} over the SEST field (i.e., N83 itself). The dashed curve shows the color-color relation expected for a modified blackbody, which is not a good description of the SMC. On the other hand, the solid and dash-dotted lines, which show the relations that we use in our analysis, can reasonably predict I_{100}/I_{160} from I_{70}/I_{160} .

approach reproduces optical and near-IR extinction in Galactic molecular clouds, though with some systematic uncertainties.

Figure 2 motivates our use of I_{70}/I_{160} (x -axis) to predict I_{100}/I_{160} (y -axis). Gray contours show the distribution of data for the whole SMC. Bins (filled circles) show data from a 2° square field centered on N83 (i.e., Figure 1). Both near N83 and over the whole SMC, the two colors show a reasonable correlation (rank correlation coefficient 0.7).

Figure 2 also motivates our *ad hoc* treatment of the conversion between I_{70}/I_{160} and I_{100}/I_{160} . A single modified blackbody (the dashed line shows one with $\beta = 1.5$) cannot simultaneously describe the SMC at 70 , 100 , and $160\mu\mathrm{m}$. The simplest explanation is that I_{100}/I_{160} traces T_{dust} , while the $70\mu\mathrm{m}$ band includes substantial non-equilibrium emission. We tested the possibility of using the models of Draine & Li (2007), which include the effects of stochastic heating, to directly derive dust masses from I_{70}/I_{160} . However, the currently available “SMC” models cannot reproduce the data in Figure 2. Bot et al. (2004) and Bernard et al. (2008) showed that a similar case holds for the Desert et al. (1990) models. The main stumbling block is reproducing the observed $60\mu\mathrm{m}$ (Desert et al. 1990) or $70\mu\mathrm{m}$ (Draine & Li 2007) emission.

Equation 3 is not a unique description. A simple alternative is a modified blackbody with twice the expected emission at $70\mu\mathrm{m}$. In this case:

$$\frac{I_{70}}{I_{160}} = 2.0 \times \left(\frac{70}{160}\right)^{-1.5} \frac{B_{\nu}(T_{\mathrm{dust}}, 70\mu\mathrm{m})}{B_{\nu}(T_{\mathrm{dust}}, 160\mu\mathrm{m})}, \quad (4)$$

This is shown by the dash-dotted line in Figure 2. It reproduces the data near N83 with about the same

accuracy as Equation 3. If equilibrium emission sets I_{100}/I_{160} , then Equation 4 implies that other processes (e.g., single-photon heating of small grains) contribute $\approx 50\%$ of the emission at $70\mu\text{m}$ near N83 (and across the whole SMC). This is in reasonable agreement with the results for the Solar Neighborhood and several nearby GMCs (Desert et al. 1990; Schnee et al. 2005, 2008).

The aim of this paper is not to investigate the details of small grain heating in the SMC, so we move forward using our empirical fit (Equation 3). This appears as a solid line in Figure 2. It is a good match to the data near N83, where the RMS scatter in the color of individual pixels about the fit is ≈ 0.04 . In deriving uncertainties we use Equation 4 as an equally valid alternative to Equation 3.

To convert from I_{100}/I_{160} to T_{dust} we assume that the SED along each line of sight is described by a modified blackbody with $\tau_\lambda \propto \lambda^{-\beta}$. At long wavelengths ($\lambda \gtrsim 100\mu\text{m}$), a blackbody spectrum with a wavelength-dependent emissivity is indeed a good description of the integrated SED of the SMC (Aguirre et al. 2003; Wilke et al. 2004; Leroy et al. 2007). We take $\beta = 1.5$, which is intermediate in the range of plausible values (e.g., Draine & Lee 1984) and a reasonable description of the integrated SMC SED from $\lambda \sim 100\text{--}1000\mu\text{m}$. This is not strongly preferred, and so we allow β from 1.0 to 2.0 in our assessment of uncertainties.

3.2. Uncertainties in τ_{160}

We assess the uncertainty in τ_{160} by repeatedly adding realistic noise to our 70 and $160\mu\text{m}$ data and then deriving τ_{160} under varying assumptions. For each realization, we offset the observed 70 and $160\mu\text{m}$ maps by a random amount to reflect uncertainty in the background subtraction; these offsets are drawn from normal distributions with $1\sigma = 0.25 \text{ MJy ster}^{-1}$ at $70\mu\text{m}$ and 1 MJy ster^{-1} at $160\mu\text{m}$. We add normally distributed noise to each map. This noise has amplitude equal to the measured noise (§2) and is correlated on scales of $36''$.

We derive I_{100}/I_{160} for each realization using either the polynomial fit (Equation 3) or scaling the $70\mu\text{m}$ intensity (Equation 4), with equal probability of each. We add normally distributed noise to I_{100}/I_{160} with $1\sigma = 0.04$ (the RMS residual about Equations 3 and 4) and then derive T_{dust} assuming β anywhere from 1.0 to 2.0 with equal probability.

This entire process is repeated 1,000 times. We use the distribution of Monte Carlo τ_{160} s for each pixel to estimate a realistic uncertainty, finding individual measurements to be uncertain by $\approx 40\%$ (1σ). We extend the same approach through our derivation of $N(\text{H}_2^{\text{FIR}})$ in §4.4. In Appendix A we discuss systematic effects that cannot be straightforwardly incorporated into this approach, two of which (blended dust populations and hidden cold dust) could impact τ_{160} .

3.3. τ_{160} and Extinction

It will be useful to make an approximate assessment of the dust column in terms of V -band line-of-sight extinction, A_V , and reddening, $E(B - V)$. In the Solar Neighborhood, $E(B - V) = N(\text{H})/5.8 \times 10^{21} \text{ cm}^{-2}$ (Bohlin et al. 1978) and $\tau_{160} = 2.44 \times 10^{-25} \text{ cm}^2 N(\text{H I})$ (Boulanger et al. 1996, studying the Galactic cirrus where we may safely assume that $N(\text{H}) \approx N(\text{H I})$). Then

$$E(B - V) [\text{mag}] \approx 710 \tau_{160}. \quad (5)$$

The reddening law in the SMC yields $R_V \approx 2.7$ (Bouchet et al. 1985; Gordon et al. 2003), so that

$$A_V [\text{mag}] = 1910 \tau_{160} \quad (6)$$

These equations assume the emissivity, $\tau_{160}/E(B - V)$, of Galactic H I but do not depend on the specific dust-to-gas ratio.

Estimates of A_V and $E(B - V)$ based on τ_{160} and Equations 5 and 6 agree well with optical- and UV-based measurements. Caplan et al. (1996) compiled A_V for a number of SMC H II regions, including N83 and N84A/B (both of which lie within the SEST field). Towards N83 they find A_V in the range $0.42\text{--}0.79$ mag (mean 0.63 mag); towards N84A/B they found A_V from $0.24\text{--}0.60$ mag (mean 0.37 mag). Using their positions and aperture sizes, we derive $A_V = 1.34 \pm 0.36$ mag and 0.93 ± 0.26 mag for the same regions. The optical and UV measurements are based on absorption toward sources inside the SMC. Therefore they will sample half the total line-of-sight extinction on average. Accounting for this, our FIR-based extinction estimates are in excellent agreement with optical values. We find the same good agreement for Sk 159, a B star near N83 towards which Fitzpatrick (1984) and Tumlinson et al. (2002) measured $E(B - V) \approx 0.05$ mag, while we estimate $E(B - V) = 0.08 \pm 0.03$ mag (see §4.3).

4. DUST AND GAS NEAR N83

Following the method described in §3, we calculate τ_{160} over every line of sight in a 2° field centered on N83 (Figure 1) and in the SEST field. In the process, we derive a median $T_{\text{dust}} = 20.9 \pm 1.5$. This agrees with the $T = 22 \pm 2$ K found by Bot et al. (2004) for dust in the SMC Wing. The temperature in the N83 complex is somewhat higher, with median $T_{\text{dust}} = 22.9 \pm 1.5$ K and values up to $\sim 28 \pm 2$ K. The hottest regions are coincident with the N83, N84A, and N84B H II regions.

Our goal in this section is to combine τ_{160} with the measured $N(\text{H I})$ to estimate $N(\text{H}_2)$ via

$$N(\text{H}_2^{\text{FIR}}) = \frac{1}{2} \left(\frac{\tau_{160}}{DGR} - N(\text{H I}) \right). \quad (7)$$

Here DGR is the dust-to-gas ratio defined by

$$\tau_{160} = DGR N(\text{H}) [\text{cm}^{-2}], \quad (8)$$

$N(\text{H}) = N(\text{H I}) + N(\text{H}_2)$, and H_2^{FIR} refers to the distribution of H_2 derived using this approach. To calculate H_2^{FIR} , we first compare τ_{160} and $N(\text{H I})$ in the area around N83 where the ISM is likely to be mostly H I (§4.1). This demonstrates that τ_{160} effectively traces the ISM and allows us to directly measure DGR in the diffuse ISM. We show that residuals about this $\tau_{160}\text{-}N(\text{H I})$ relation come exclusively from regions of active star formation (§4.2). We then adopt a reasonable value for the DGR in N83 itself and estimate $N(\text{H}_2)$ across the complex.

4.1. H I and Dust Near N83

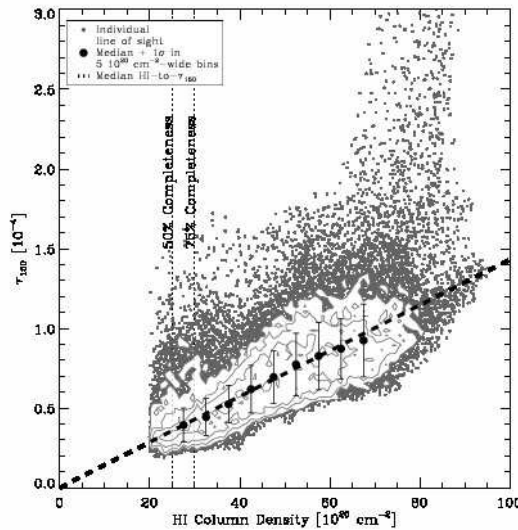


FIG. 3.— Dust column, traced by τ_{160} , (y-axis) as a function of H I column density (x-axis) in a 2° field centered on N83. Black circles show average τ_{160} and 1σ variation in bins $5 \times 10^{20} \text{ cm}^{-2}$ wide. The dashed line shows the median ratio $\tau_{160}/N(\text{H I}) = 1.4 \times 10^{-26} \text{ cm}^2$. Dotted lines show the H I column density for which 50 and 75% of the pixels are well above the background (see §2.1; only such points are plotted). Contours show the distribution of data where point density is very high; the contour increment is a factor of two in data density. Dust and gas are reasonably related by a linear scaling over most of the field. The deviations to high τ_{160} mostly coincide with N83 and other sites of active star formation.

In Figure 3, we plot τ_{160} as a function of $N(\text{H I})$ over the 2° field centered on N83. Most of the data are well-described by

$$\tau_{160} = 1.4_{-0.5}^{+0.8} \times 10^{-26} \text{ cm}^2 N(\text{H I}) [\text{cm}^{-2}] , \quad (9)$$

which is shown by the dashed line in Figure 3. We expect that $N(\text{H}) \approx N(\text{H I})$ over most of this area. Thus, the clear, linear correlation in Figure 3 demonstrates that τ_{160} traces the ISM well here and the slope is an estimate of the *DGR* in the diffuse ISM of the SMC Wing.

Equation 9 is consistent within the uncertainties with results of Bot et al. (2004), who found $\tau_{160} \approx (1.0 \pm 0.5) \times 10^{-26} \text{ cm}^2 N(\text{H I}) [\text{cm}^{-2}]$ for the whole Wing (after adjusting for slight differences in T_{dust} , β , and λ). In the Solar Neighborhood, $\tau_{160} \approx 2.44 \times 10^{-25} \text{ cm}^2 N(\text{H I}) [\text{cm}^{-2}]$ (Boulanger et al. 1996). Comparing this to Equation 9 implies that the *DGR* near N83 is 17_{-6}^{+10} times smaller than the Galactic value. This agrees within the uncertainties with the *DGR* found for the SMC Wing by Leroy et al. (2007), which is $\approx 10_{-5}^{+10}$ lower than Galactic¹⁰.

From Equations 9 and 5, we estimate $N(\text{H})/E(B-V) \approx 10_{-4}^{+6} \times 10^{22} \text{ cm}^{-2} \text{ mag}^{-1}$. This matches the SMC-average $N(\text{H})/E(B-V) \approx 8.7 \times 10^{22} \text{ cm}^{-2} \text{ mag}^{-1}$ measured by Fitzpatrick (1985) using IUE and confirmed by Tumlinson et al. (2002) with FUSE.

4.2. Residuals About the τ_{160} -H I Relation

¹⁰ Leroy et al. (2007) made no correction for H I opacity. Doing so would improve the agreement with the present measurement.

Equation 9 and Figure 3 demonstrate that a single *DGR* describes the region near N83 well. The notable exceptions are a small number of points with high τ_{160} relative to their H I column density. In Figure 4 we show the distribution of residuals about Equation 9. Contours indicate where our Monte Carlo uncertainty estimates yield 85, 98, and 99.9% confidence that the residuals are really greater than zero.

The neighboring panel shows the same confidence contours superimposed on an H α image of the region near N83 (Winkler et al., private communication). The highest residuals are associated with N83 itself. Other regions with higher-than-expected τ_{160} are also associated with concentrations of H α emission. H α emission indicates ongoing massive star formation, which in turn suggests the presence of H₂. N83 also has significant CO emission, another signpost of H₂ (Mizuno et al. 2001). If a large amount of the ISM is H₂, we expect high residuals about Equation 9 even for a fixed *DGR*.

4.3. The Dust-to-Gas Ratio in N83

To derive H₂^{FIR} from Equation 7 over the SEST field, we must know the *DGR* in N83 itself. We cannot measure this directly because we do not have an independent measure of the H₂ column. We might expect *DGR* in N83 to differ somewhat from that in the surrounding diffuse gas of the Wing: stars are more likely to form in regions with high *DGR* and the denser environment may shelter grains from destruction by shocks or lead to grain growth (e.g., Dwek 1998). In addition to our measurement of the diffuse ISM, we consider two pieces of evidence when adopting a *DGR* to use in N83: observations of a nearby B star and the metallicity of the N84C H II region.

FUSE and IUE Measurements of Sk 159: From FUSE and IUE absorption measurements, $E(B-V)$, $N(\text{H}_2)$, and $N(\text{H I})$ are known towards Sk 159, a B0.5 star near N83 (marked by a star in Figure 4). H₂ is detected but the column density is small ($\approx 2 \times 10^{19} \text{ cm}^{-2}$, André et al. 2004). The reddening associated with the SMC is ≈ 0.05 mag (Fitzpatrick 1984; Tumlinson et al. 2002), though somewhat uncertain. The H I column measured from absorption along the same line of sight is $2 \pm 1 \times 10^{21} \text{ cm}^{-2}$ (Bouchet et al. 1985), roughly half of the column inferred from 21 cm emission along the line of sight (two kinematically distinct H I components are visible in emission towards Sk 159; only one of them is seen in absorption, implying that Sk 159 sits between the two, behind the smaller one). These values imply $N(\text{H})/E(B-V) \approx 2-6 \times 10^{22} \text{ cm}^{-2} \text{ mag}^{-1}$, or *DGR* $\approx 2-7 \times 10^{-26} \text{ cm}^2$.

Metallicity of N84C: Russell & Dopita (1990) measured the nebular metallicity of the N84C H II region, which lies within the SEST field, finding $12 + \log \text{O/H} = 8.27$, 2–3 times lower than the Solar Neighborhood value and among the highest for any region in the SMC. Translating metallicity into a *DGR* is not totally straightforward, because the fraction of heavy elements tied up in dust may vary with environment. For a fixed fraction of heavy elements in dust, one would expect $\text{DGR} \propto Z^{-1}$. Fits to samples of galaxies yield power law relationships ($\text{DGR} \propto Z^\alpha$) with indices in the range $\alpha = 1-2$ (e.g., Lisenfeld & Ferrara 1998; Draine et al. 2007). This

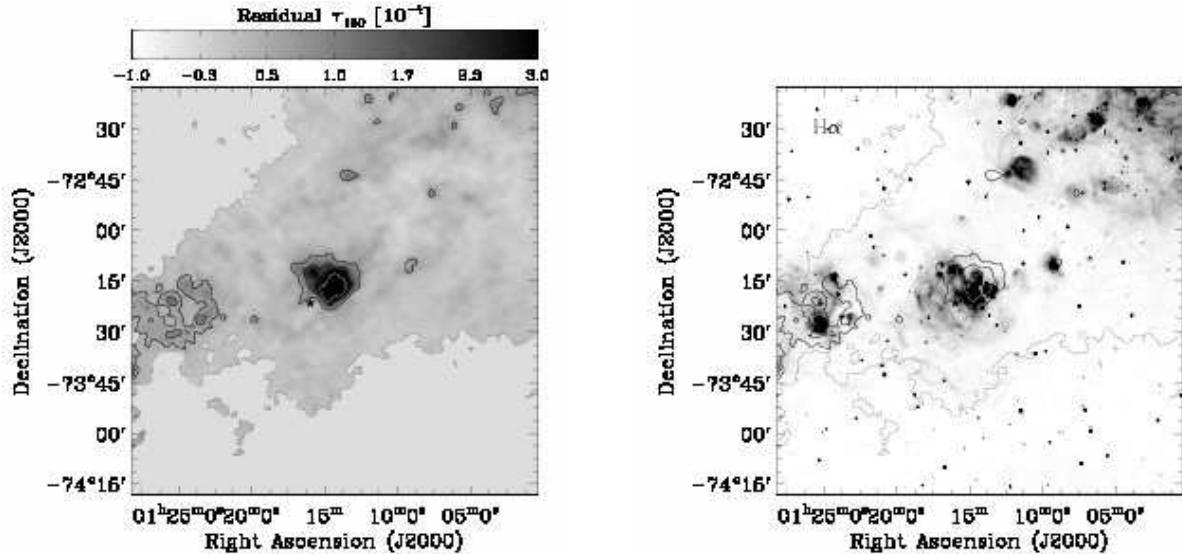


FIG. 4.— (left) Residuals about Equation 9, the average relationship between τ_{160} and H I in a 2° field centered on N83. The contours show where our Monte Carlo uncertainty estimate yields 85, 98, and 99.9% confidence that the residual is above zero. A thin gray line shows where we clearly distinguish FIR emission from the background (see §2.1) and the star indicates Sk 159, a B star observed by FUSE and IUE. Most of the region is well-described by Equation 9, but N83 itself shows higher τ_{160} than expected from H I and Equation 9. (right) The same contours plotted on top of H α emission near N83. Regions with high τ_{160} residuals are associated with sites of recent high-mass star formation.

would imply $N(\text{H})/E(B-V) \sim 2-7 \times 10^{22} \text{ cm}^{-2} \text{ mag}^{-1}$ or $DGR \sim 2-7 \times 10^{-26} \text{ cm}^2$.

H I and τ_{160} : Equation 9 offers a lower bound on the DGR — N83 is extremely unlikely to have a lower DGR than the surrounding medium ($N(\text{H})/E(B-V) \approx 10 \times 10^{22} \text{ cm}^{-2} \text{ mag}^{-1}$) and from absorption work we know that there is not a pervasive massive molecular component in the SMC. The magnitude of the residuals about this equation towards N83 itself also offer a weak upper bound on the quantity. If we assume DGR much above 3 times the value in Equation 9 then some lines of sight inside the SEST field will have significantly *negative* residuals. If the star-forming region itself is described by a single DGR , then it must be roughly bounded by this value, which translates to $N(\text{H})/E(B-V) \sim 3 \times 10^{22} \text{ cm}^{-2} \text{ mag}^{-1}$.

Assumed DGR in N83: The relatively high metallicity and the measurement towards Sk 159 are balanced against our observations of a very low DGR in the nearby ISM and the requirement that $\Sigma_{\text{H}_2}^{\text{FIR}}$ not be significantly and systematically negative. The former suggest $N(\text{H})/E(B-V) \sim 2-7 \times 10^{22} \text{ cm}^{-2} \text{ mag}^{-1}$, while the latter yields $N(\text{H})/E(B-V) \sim 3-10 \times 10^{22} \text{ cm}^{-2} \text{ mag}^{-1}$. In the remainder of this paper we adopt assume that in N83 itself $N(\text{H})/E(B-V) \sim 5 \times 10^{22} \text{ cm}^{-2} \text{ mag}^{-1}$, which is intermediate in this range. Then

$$\tau_{160} = 2.8 \times 10^{-26} \text{ cm}^2 N(\text{H}) [\text{cm}^{-2}] . \quad (10)$$

This is twice the value found in the diffuse gas of the SMC Wing (Equation 9) and more similar to that found in the actively star-forming SMC Bar (e.g., Wilke et al. 2004; Leroy et al. 2007). It is roughly consistent with observations of Sk 159 and the metallicity of N84C. This DGR also leads to reasonable agreement between dynamical and dust masses in the star-forming region (§5.4), which was a factor in settling on this value. In Appendix A we

illustrate the effects of changing this value on our analysis.

4.4. H_2^{FIR} in N83

Combining Equations 7 and 10 we estimate $N(\text{H}_2^{\text{FIR}})$ from τ_{160} and $N(\text{H I})$. From $N(\text{H}_2^{\text{FIR}})$, we calculate the molecular gas surface density,

$$\Sigma_{\text{H}_2}^{\text{FIR}} [\text{M}_\odot \text{ pc}^{-2}] = \frac{N(\text{H}_2^{\text{FIR}})}{4.6 \times 10^{19} [\text{cm}^{-2}]} , \quad (11)$$

which includes a factor of 1.36 to account for helium¹¹ (after Wilson et al. 1988). At the same time we estimate the extinction along each line of sight using Equation 6. Carrying out these calculations, we work with $N(\text{H I})$ only in average, because the resolution of the 160 μm and CO $J = 2 \rightarrow 1$ data are $\sim 38''$, while that of the H I map is 98'' (§2.2).

The right column in Figure 5 shows the resulting maps of $\Sigma_{\text{H}_2}^{\text{FIR}}$ in N83 at the resolution of the SEST CO 2 \rightarrow 1 (top) and 1 \rightarrow 0 (bottom) data. The left column shows the CO maps. Note that the stretch on the H_2^{FIR} images runs linearly from $\Sigma_{\text{H}_2}^{\text{FIR}} = 100 \text{ M}_\odot \text{ pc}^{-2}$ to $500 \text{ M}_\odot \text{ pc}^{-2}$.

Several systematic uncertainties may affect $N(\text{H}_2^{\text{FIR}})$ but are hard to quantify and so not reflected in our Monte Carlo estimate of the uncertainties. We consider these in Appendix A, finding no strong reason to doubt that Equation 7 yields an approximate estimate of $N(\text{H}_2)$.

5. H_2^{FIR} , CO, DUST, AND DYNAMICS

5.1. H_2^{FIR} and H I

¹¹ In the rest of the paper, $\Sigma_{\text{H}_2}^{\text{FIR}}$ includes this correction for helium, while $N(\text{H}_2)$ or $N(\text{H}_2^{\text{FIR}})$ refer to column density of H_2 alone

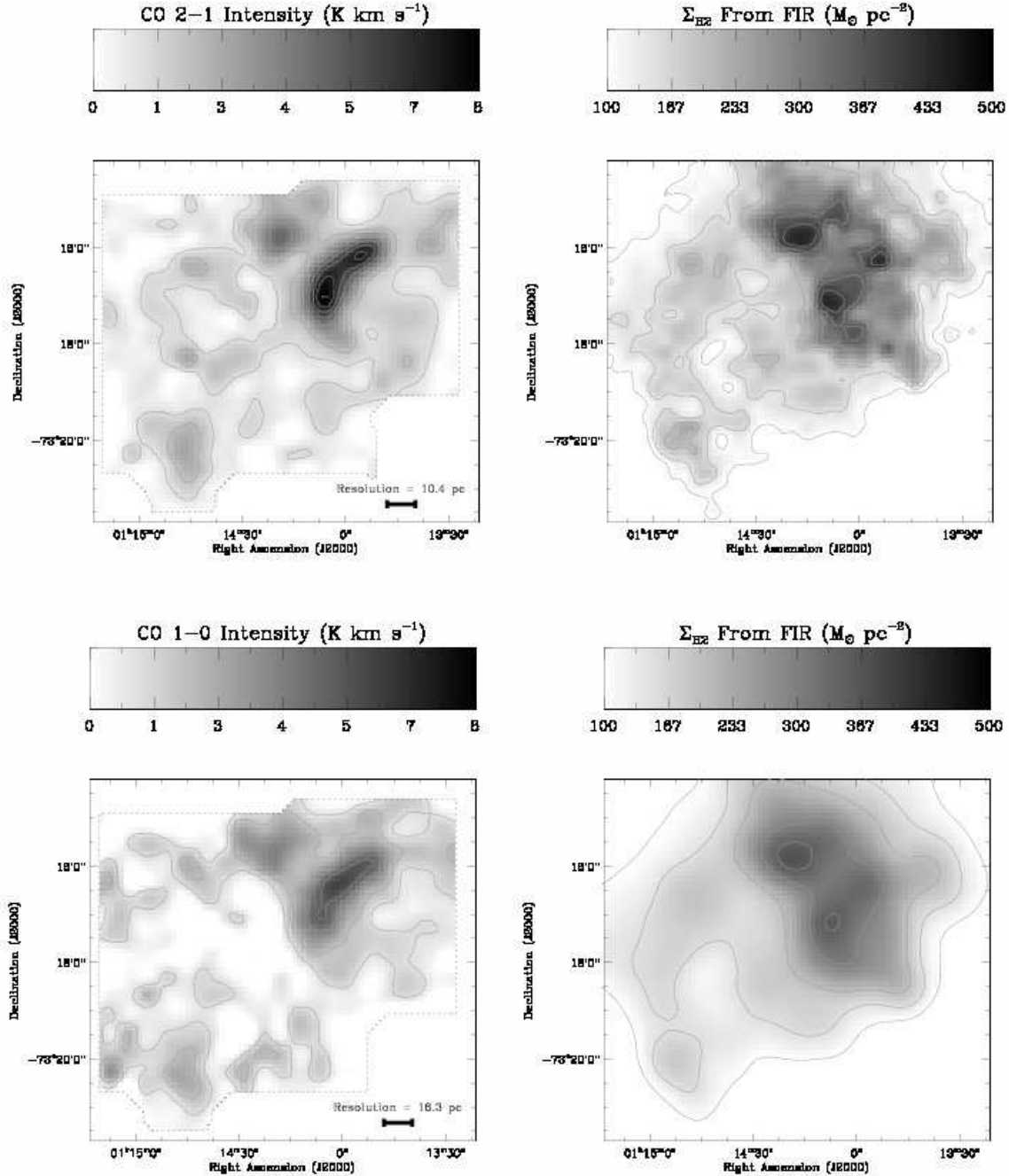


FIG. 5.— CO emission (left panels) and $\Sigma_{\text{H}_2}^{\text{FIR}}$ estimated using Equation 7 (right panels). The top panels show CO $J = 2 \rightarrow 1$ emission and H_2^{FIR} at $\sim 38''$ resolution (but see §2.2 regarding the resolution of the H_2^{FIR} map). The bottom panels show CO $J = 1 \rightarrow 0$ emission and H_2^{FIR} at $55''$ resolution. Dotted contours show the boundaries of the SEST map. In the CO maps, contours show I_{CO} from 1 to 8 K km s^{-1} spaced by 1 K km s^{-1} . In the H_2^{FIR} maps, contours indicate $\Sigma_{\text{H}_2}^{\text{FIR}}$ from 100 to 500 $\text{M}_\odot \text{ pc}^{-2}$ spaced by 50 $\text{M}_\odot \text{ pc}^{-2}$.

Before we consider the relationship between CO, H_2^{FIR} , and dust within N83, we briefly examine the transition from atomic (H I) to molecular (H_2) gas in the complex.

Krumholz et al. (2009) recently considered the transition from H I to H_2 in galaxies. They argue that inside a complex of mixed atomic and molecular gas, the ratio of H_2 to H I along a line of sight ($R_{\text{H}_2} = \Sigma_{\text{H}_2}/\Sigma_{\text{HI}}$) is mainly a function of two factors: total gas surface density ($\Sigma_{\text{HI}} + \Sigma_{\text{H}_2}$) and metallicity. Their calculations agree

well with a variety of observations, including FIR-based estimates of Σ_{H_2} in the SMC at lower resolution.

Comparing H I and H_2 in the area around N83, we indeed observe a clear relationship between R_{H_2} and the total gas surface density. We show this in Figure 6, plotting R_{H_2} against $\Sigma_{\text{HI}} + \Sigma_{\text{H}_2}^{\text{FIR}}$ over the whole area where $\Sigma_{\text{H}_2}^{\text{FIR}} > 0$. We work at the $98''$ (29 pc) resolution of the H I map, with each point in the plot showing an independent measurement. For this analysis, we are interested

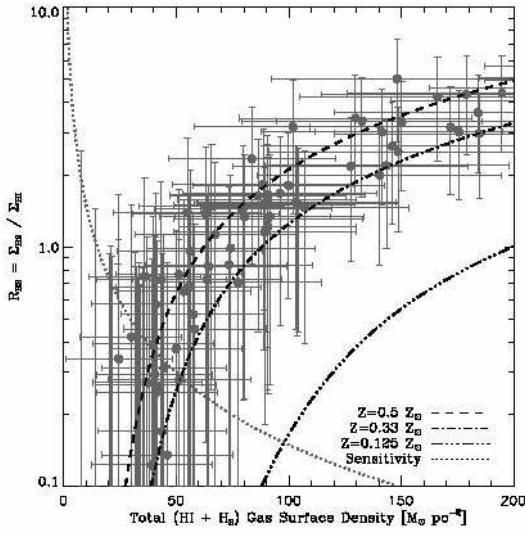


FIG. 6.— Ratio of molecular to atomic gas, $R_{\text{H}_2} = \Sigma_{\text{H}_2}^{\text{FIR}} / \Sigma_{\text{HI}}$, as a function of total gas column density $\Sigma_{\text{HI}} + \Sigma_{\text{H}_2}$ in the N83 complex (after removing H I not associated with the complex). Each point shows an independent measurement at 29 pc resolution. The dotted line shows the sensitivity of our H_2^{FIR} map. We plot the theoretical relationships between R_{H_2} and $\Sigma_{\text{HI}} + \Sigma_{\text{H}_2}$ calculated by Krumholz et al. (2009) for several metallicities.

in the gas associated with the star-forming complex itself (not unassociated gas in front of and behind it along the line of sight). To remove H I unassociated with N83 itself from Σ_{HI} , we subtract the median Σ_{HI} measured over the area shown in Figure 1 ($53 \text{ M}_\odot \text{ pc}^{-2}$) from the measured Σ_{HI} before plotting. This is only an issue for H I; H_2^{FIR} does not extend beyond the N83 complex.

We overplot the relationship between R_{H_2} and $\Sigma_{\text{HI}} + \Sigma_{\text{H}_2}$ predicted by Krumholz et al. (2009) for three metallicities: $Z = 0.5, 0.33$, and 0.125 times solar. Our data are consistent with the shape of the Krumholz et al. (2009) calculation. We find $R_{\text{H}_2} = 1$ at $\Sigma_{\text{H}_2} + \Sigma_{\text{HI}} = 68 \pm 12 \text{ M}_\odot \text{ pc}^{-2}$, which agrees well with their calculations for Z 2-3 times lower than the solar value. This is roughly the metallicity measured for the N84C H II region (Russell & Dopita 1990). However, it is significantly higher than the *DGR* that we adopt (§4.3), which is closer to the lower value. Because Krumholz et al. (2009) assume a linear scaling between dust opacity and metallicity when deriving these curves, this means that there remains some disagreement between our measurements and their results. Nonetheless, there is good qualitative agreement in the shape of the curve and the fact that in N83 $R_{\text{H}_2} = 1$ at a significantly higher value of $\Sigma_{\text{HI}} + \Sigma_{\text{H}_2}$ than in a solar metallicity cloud.

5.2. CO and H_2^{FIR}

Figure 5 shows that the distributions of H_2^{FIR} and CO share the same peaks and basic morphology. However, the values of I_{CO} in N83 are low compared to a Galactic molecular cloud, which usually show $I_{\text{CO}} \sim 10 \text{ K km s}^{-1}$ over a large area, not merely the peaks (e.g., Wilson et al. 2005). By contrast, the values of $\Sigma_{\text{H}_2}^{\text{FIR}}$ (mean $180 \text{ M}_\odot \text{ pc}^{-2}$) are similar to the surface density of an average Galactic GMC $\sim 120\text{--}170 \text{ M}_\odot \text{ pc}^{-2}$ (Solomon et al. 1987; Heyer et al. 2008).

This means that CO is faint compared to H_2^{FIR} in N83.

Over the SEST field X_{CO} is

$$\langle X_{\text{CO}}^{2 \rightarrow 1} \rangle = 6.7_{-2.6}^{+2.8} \times 10^{21} \frac{\text{cm}^{-2}}{\text{K km s}^{-1}} \quad (12)$$

$$\langle X_{\text{CO}}^{1 \rightarrow 0} \rangle = 7.9_{-2.8}^{+4.2} \times 10^{21} \frac{\text{cm}^{-2}}{\text{K km s}^{-1}}$$

These ratios are 34 and 40 times the Galactic conversion factor, taken to be $X_{\text{Gal}} \approx 2 \times 10^{20} \text{ cm}^{-2} (\text{K km s}^{-1})^{-1}$ (e.g., Strong & Mattox 1996; Dame et al. 2001). This value agrees reasonably with previous FIR-based determinations of X_{CO} in the SMC and N83: comparing IRAS and CO at selected pointings in the SMC, Israel (1997b) derived $X_{\text{CO}} \sim 67 X_{\text{Gal}}$. Applying the same methodology to N83, Bolatto et al. (2003) found $X_{\text{CO}} \sim 100 \pm 50 X_{\text{Gal}}$. Leroy et al. (2007) derived $X_{\text{CO}} \sim 50 X_{\text{Gal}}$ comparing NANTEL CO, IRIS $100 \mu\text{m}$ and *Spitzer* $160 \mu\text{m}$ towards N83 (removing their correction for extent).

The left panel in Figure 7 compares H_2^{FIR} and I_{CO} for individual lines of sight. We plot $\Sigma_{\text{H}_2}^{\text{FIR}}$ as a function of I_{CO} over the SEST field. We regrid the data so that each point corresponds to an approximately independent measurement over a $\sim 10 \text{ pc}$ (CO $J = 2 \rightarrow 1$) or $\sim 17 \text{ pc}$ (CO $J = 1 \rightarrow 0$) wide box. Gray curves show fixed CO-to- H_2 conversion factors, starting with Galactic (lowest) and increasing by factors of 3.33.

As with Figure 5, Figure 7 shows that despite the very low ratio of CO to H_2^{FIR} , the two exhibit an overall correspondence. High I_{CO} coincides with high $\Sigma_{\text{H}_2}^{\text{FIR}}$ and the reverse, so that a rank correlation coefficient of 0.7 relates the two over the SEST field.

The relationship between I_{CO} and $\Sigma_{\text{H}_2}^{\text{FIR}}$ does not go through the origin. Instead, $I_{\text{CO}} = 0$ corresponds to roughly $\Sigma_{\text{H}_2}^{\text{FIR}} = 50\text{--}150 \text{ M}_\odot \text{ pc}^{-2}$. This suggests the presence of an envelope of H_2^{FIR} with very little or no associated CO. Unfortunately, this result is very sensitive to the adopted *DGR* (§4.3 and Appendix A). If we take *DGR* at the upper end of the plausible range, the data are consistent with no CO-free envelope although CO emission is still faint relative to $\Sigma_{\text{H}_2}^{\text{FIR}}$ in the SEST field. If we take *DGR* at the value derived in the nearby diffuse ISM, the surface density of the envelope is even higher $\sim 200\text{--}400 \text{ M}_\odot \text{ pc}^{-2}$. Although the observation towards Sk 159 does not actually intersect the envelope in the latter case, it is very nearby and the low $N(\text{H}_2)$ derived from absorption towards this star offers some circumstantial evidence against a very massive extended envelope.

The other notable feature of this plot is that at very high $\Sigma_{\text{H}_2}^{\text{FIR}}$ CO intensity increases dramatically (the turn to the right at the top of the plot). We see this in both CO transitions, but the effect is more pronounced at the higher resolution of the CO $J = 2 \rightarrow 1$ data, suggesting that the bright CO-emitting structures are still relatively small compared to the SEST beam. The result is that the line-of-sight integrated ratio of H_2^{FIR} to CO is lower for the regions of brightest CO emission, dropping to ~ 15 times the Galactic value. Care must be taken interpreting these ratios because H_2^{FIR} and CO emission almost certainly trace different volumes (§5.4).

5.3. CO and Extinction

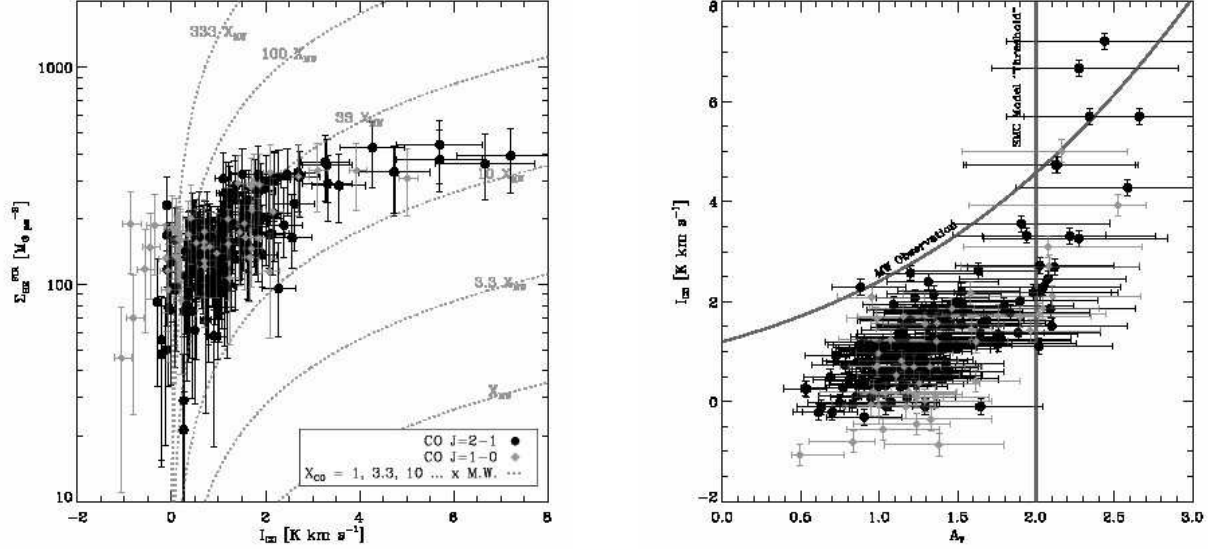


FIG. 7.— The structure of H_2 , CO, and dust in N83. (left) H_2^{FIR} surface density, $\Sigma_{\text{H}_2}^{\text{FIR}}$, as a function CO intensity, I_{CO} (x -axis). Dotted gray lines show CO-to- H_2 conversion factors of 1, 3.33, 10 ... 333 times the Galactic value. (right) I_{CO} (y -axis) as a function of line-of-sight extinction, A_V (x -axis), estimated from τ_{160} . The vertical line shows the line-of-sight extinction from which most CO emission emerges in models of SMC molecular clouds by Lequeux et al. (1994). The gray curve shows the relationship between I_{CO} and extinction observed in the Pipe Nebula (Milky Way) by Lombardi et al. (2006). In both plots, each data point represents an independent line of sight. We show results for the $J = 2 \rightarrow 1$ transition (38'' resolution) in black and the $J = 1 \rightarrow 0$ transition (55'' resolution) in gray.

In §1, we highlighted the role of dust in shielding CO from dissociating radiation. This may provide a simple explanation for the upturn in CO intensity at high $\Sigma_{\text{H}_2}^{\text{FIR}}$. Lequeux et al. (1994) modeled CO emission in SMC molecular clouds. For their typical cloud ($n_{\text{H}} \sim 10^4 \text{ cm}^{-3}$, illuminated by a radiation field 10 times the local interstellar radiation field), they found that most CO emission comes from a relatively narrow region of the cloud centered on $A_V \sim 1$ mag. Outside this regime CO intensity is very weak, a scenario that qualitatively matches what we see in the left panel of Figure 7 (see also Bell et al. 2006).

In the right panel of Figure 7 we plot CO intensity as a function of line-of-sight extinction, A_V . We estimate A_V from τ_{160} using Equation 6. For comparison, we mark $A_V \sim 2$ mag, the line-of-sight extinction that roughly matches the depth from which Lequeux et al. (1994) predict most CO emission to emerge (see their Figures 2 and 6). They model a slab illuminated from one side while we estimate the total extinction along the line of sight through the cloud. Therefore $A_V = 1$ mag for them corresponds to $A_V \sim 2$ mag for us (though the actual geometry is likely to be much more complicated). We also plot the relationship between extinction and CO intensity measured in the Pipe Nebula (a nearby Milky Way cloud) by Lombardi et al. (2006, see their Figure 22). We convert A_K into A_V using their adopted $A_V = A_K/0.112$. They measure a scatter of roughly 2 K km s^{-1} about this relation.

In agreement with Lequeux et al. (1994), we find that lines of sight with bright CO emission occur almost exclusively above $A_V \sim 2$ mag. Our maps lack the dynamic range in A_V to test whether I_{CO} is indeed more or less independent of extinction well above this threshold (as in the Milky Way, Lombardi et al. 2006; Pineda et al. 2008). In fact, Figure 3a of Lequeux et al. (1994) seems a close match to what we observe: a shallow slope that

steepens sharply around A_V of 2 mag (for us). The radiation field that they assume, 10 times the Galactic value is a rough match to what one would infer comparing T_{dust} in N83 (median ~ 23 K, max ~ 28 K) to that of Galactic cirrus (17.5 K) — median ~ 5 , maximum $\sim 15^{12}$ — especially when one recalls that this is integrated over the whole line of sight rather than tracing the radiation field incident on the cloud surface.

N83 shows somewhat less CO at a given extinction than the Pipe Nebula. This is also in agreement with the models by Lequeux et al. (1994), which predict that CO from Milky Way clouds emerges from a broader range of A_V and lower values of A_V than in the SMC. They attribute the difference to lower rates of photodissociation and it certainly seems likely that the radiation field incident on the H_2 in N83 is much more intense than in the relatively quiescent Pipe.

Small differences should not overshadow the similarities between the CO-extinction relation in the Milky Way and that in the SMC. Compared to the left panel in Figure 7, the right panel actually shows a striking similarity between Galactic and SMC clouds. We derive a CO- H_2 conversion that differs with the Milky Way by a factor of ~ 30 , while the relationship between extinction and CO is only slightly offset. Figure 7 supports the hypothesis that shielding, rather than the distribution of H_2 , determines the location of bright CO emission. Here “shielding” refers to a combination of dust and self-shielding. Both processes are important to setting the location at which most C is tied up in CO (e.g., Wolfire et al. 1993) and the effective shielding from both sources will be weaker in the SMC than in the Galaxy due to the decreased metallicity.

Extinction may also be critical to a cloud’s ability to

¹² For our adopted $\beta = 1.5$, the magnitude of the radiation field heating the dust is roughly $\propto T^{5.5}$.

form stars. McKee (1989) proposed that ionization by an external radiation field plays an important role in setting cloud structure because it determines the degree of magnetic support. He predicted that clouds forming low-mass stars in equilibrium will self-regulate to achieve integrated line-of-sight extinctions $A_V \approx 4\text{--}8$ mag. These extinctions are higher than the $A_V \sim 2\text{--}3$ mag that we find towards the CO peaks N83 or the average extinction over the region, $A_V \sim 1.5$ mag. We can safely conclude that the N83 region as a whole does not resemble the equilibrium low-mass star forming cloud described by McKee (1989). If these equilibrium structures do exist in this region, they must be compact relative to our 10 pc beam. Bolatto et al. (2008) find that the dynamics of CO emission in the SMC also appear to disagree with the predictions of McKee (1989) but present several important caveats to the comparison. The most important of these here is that McKee (1989) explicitly consider clouds forming only low-mass stars, while N83 is quite obviously actively producing high mass stars.

We emphasize that this comparison between CO and A_V is fairly robust. It does not depend on our choice of DGR , only on the adopted FIR emissivity (τ_{FIR}/A_V) and reddening law. The most likely biases in the emissivity (e.g., coagulation of small grains) will lower A_V , bringing our results into even closer agreement with those in the Milky Way.

5.4. H_2^{FIR} and Dynamical Mass Estimates

CO line emission also offers kinematic information. This is the basis of the virial mass method commonly used to estimate the masses of molecular clouds and derive CO-to- H_2 conversion factors (e.g. Rubio et al. 1993a; Wilson 1995; Arimoto et al. 1996), including in N83 (Bolatto et al. 2003; Israel et al. 2003; Bolatto et al. 2008). The potential pitfall of this approach may be seen from §5.3: if CO emission is confined to regions with extinction above a certain threshold and these regions represent only a fraction of the whole cloud, then velocity dispersion and size measured from CO observations will only be lower than their true values. Mass outside the region of CO emission may exert pressure on the surface of the “CO cloud,” but it is not straightforward to estimate the total mass of a cloud from observing kinematics from only part of it. As a result, in a low-metallicity cloud like N83, we expect virial masses from CO observations to be smaller than H_2^{FIR} (even over matched areas) because the latter also traces the outer (CO-free) part of the cloud, which exists in front of and behind the CO-emitting region even over matched lines of sight.

In N83, we have the advantage of an independent measurement of H_2^{FIR} and observing the CO emission over a range of scales. Here we test whether these observations can be reconciled using a simple model in which CO emission comes from only the inner part of a larger H_2 cloud (as appears to be the case in N83). We consider a spherical cloud with a radially declining density, such that $\rho \propto r^{-\alpha}$, and a radius R beyond which $\rho = 0$, i.e., the model usually adopted (with $\alpha = 1$) to calculate cloud virial masses (Solomon et al. 1987)¹³. We assume that the dynamical mass estimated from CO line data

traces the mass of a fraction of this cloud, out to radius r_{frac} . The ratio of dynamical mass to H_2^{FIR} over a matched area, $M_{\text{vir}}/M_{H_2}^{\text{FIR}}$ is then a function of α and the ratio of the true radius of the cloud to the radius of the area being considered, r_{frac}/R . The top left panel of Figure 8 shows this ratio for models with α from 0 to 2.0.

To compare our observations to this model, we measure the line width and radius of CO emission over a series of scales in N83. We consider intensity contours in position-position-velocity space, beginning with the bright northwestern region and including progressively more of the cloud (but always including that region, see Figure 8). We estimate the radius and line width of each region from the area (for the radius) and second moment (for the line width). To account for the finite resolution of SEST, the radius of each cloud is adjusted by

$$R = \sqrt{\frac{A_{\text{cloud}}}{\pi^{0.5}}} - R_{\text{beam}}^2. \quad (13)$$

Here A_{cloud} is the area of the cloud and $R_{\text{beam}} = 0.81FWHM$ is the “radius” of the beam (Solomon et al. 1987). We combine the RMS line width, σ_v , and cloud radius, R , to derive the virial mass via

$$M_{\text{vir}} = 1040R\sigma_v^2 [\text{M}_\odot], \quad (14)$$

with σ_v in km s^{-1} and R in pc. For details of measuring the properties of extragalactic GMCs from CO emission, we refer the reader to Rosolowsky & Leroy (2006) and references therein.

For each contour, we measure $M_{\text{vir}}/M_{H_2}^{\text{FIR}}$. We compare this ratio as a function of R to a range of density profiles and cloud radii. The resulting distribution of reduced χ^2 is shown in the bottom left panel of Figure 8. Our measurements, along with the best-fit model are shown in the bottom right panel of the same figure.

The best-fit model has $\rho \propto r^{-0.6}$ and $R = 70$ pc, though these numbers are not strongly constrained. The $\chi^2 = 1$ surface spans $R = 50\text{--}140$ pc and $\alpha = 0.2\text{--}0.8$. Moreover, the assumption of a virial parameter equal to 1 (i.e., that Equation 14 holds) is questionable both because we neglect support by magnetic fields, non-circular geometries, and surface pressure terms (while considering substructure inside of a larger cloud). Even more generally, the fundamental assumption that clouds or parts of clouds are virialized is not certain to hold.

Despite these concerns, Figure 8 does demonstrate that a simple model — CO emission nested inside a larger sphere of H_2 — can relate dynamics measured from molecular line emission and H_2^{FIR} . The best fit radius, $R = 70$ pc, is quite similar to that needed to achieve the extinction threshold for CO emission ($A_V \approx 1$) using our adopted DGR and $n \approx 100 \text{ cm}^{-3}$ — a typical average volume density for Galactic GMCs and perhaps appropriate for the diffuse gas between dense molecular clumps in the SMC. These three numbers combine to yield a depth of ~ 60 pc. Meanwhile, the density profile is similar to the $\alpha = 1$ commonly used to describe Galactic clouds (Solomon et al. 1987).

The strong dependence of $M_{\text{vir}}/M_{H_2}^{\text{FIR}}$ on the size-scale sampled at least partially motivates the discrepancy between CO-to- H_2 conversion factors measured us-

¹³ We cap the density at its maximum value over the inner 3% of the cloud to avoid divergence.

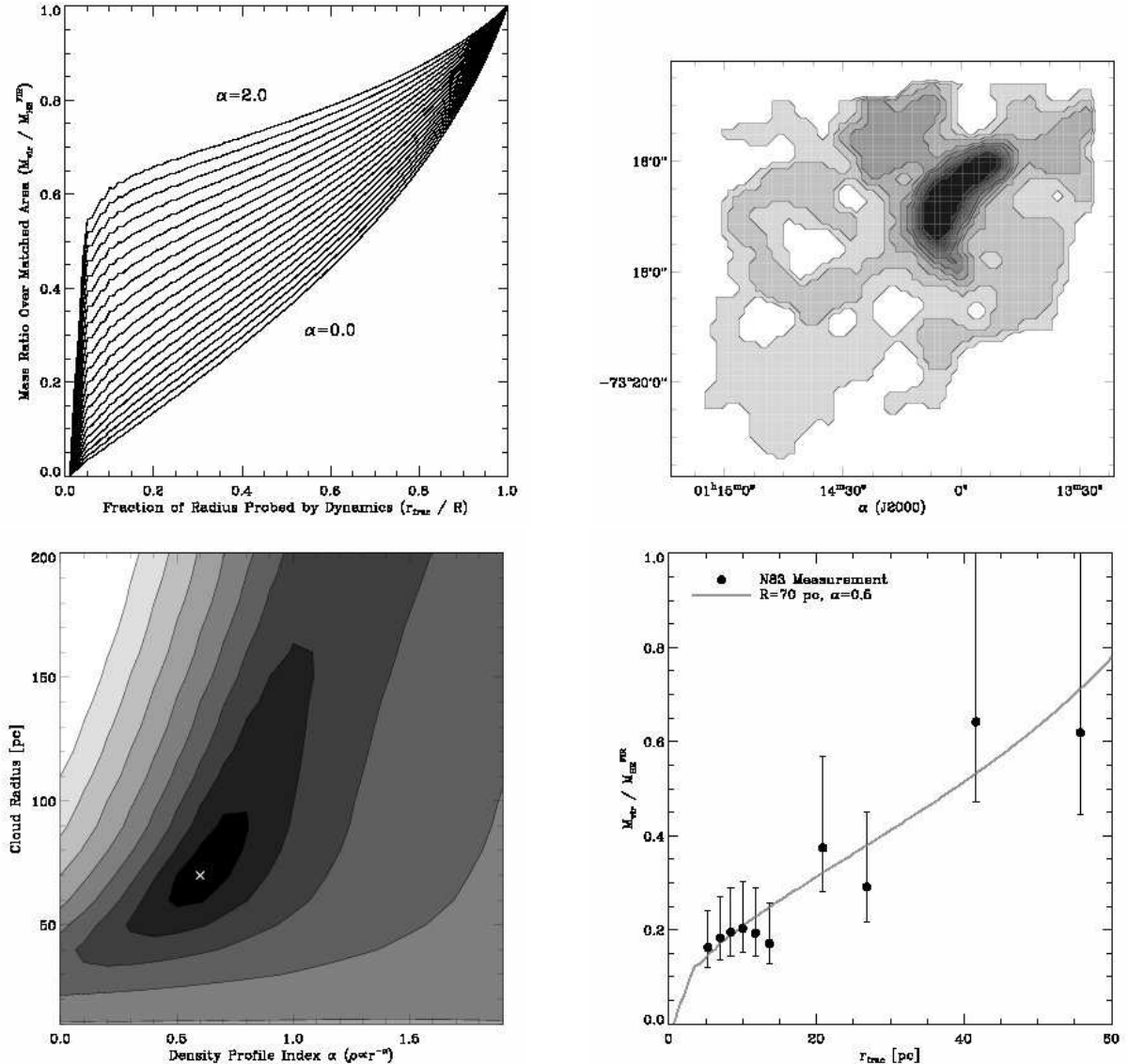


FIG. 8.— Reconciling dynamics and H_2^{FIR} in N83. (top left) The ratio of virial mass, M_{vir} , to total H_2 mass, $M_{H_2}^{\text{FIR}}$, (y -axis) expected for the simple case where M_{vir} traces only an inner portion of a cloud (the fraction traced is shown on the x -axis). Each line shows a cloud with a different density profile. (top right) N83 divided into concentric regions defined by CO intensity. We measure M_{vir} and $M_{H_2}^{\text{FIR}}$ for each region. (bottom left) Results of fitting the models in the top left panel to $M_{\text{vir}}/M_{H_2}^{\text{FIR}}$ measured from the regions in the top right panel. The x -axis show the power law index of the cloud density profile; the y -axis shows the cloud radius. Contours show reduced χ^2 , starting at 0.5 and increasing by a factor of 2 each step. The white cross marks the best-fit model ($\rho \propto r^{-0.6}$, $R = 70$ pc). (bottom right) $M_{\text{vir}}/M_{H_2}^{\text{FIR}}$ as a function of region radius (black points), along with the best fit model (gray line).

ing CO observations and those derived from dust. At the high resolutions achieved by millimeter-wave interferometers in Local Group galaxies, CO-emitting clouds are resolved from their surroundings. By concentrating on these clouds, one samples only dense regions where CO is well-shielded by dust. This naturally leads to relatively modest conversion factors. On the other hand, dust measurements and dynamical measurements made on larger scales sample the whole complex. In the SMC this appears to includes a large amount of poorly-shielded gas and such methods therefore return significantly larger conversion factors. One manifestation of this phenomenon is that dynamical mass determinations from CO measurements with larger physical beam sizes often return systematically and significantly higher

conversion factors than those obtained from CO measurements in much smaller beams (Rubio et al. 1993b; Wilson 1995; Israel 2000; Bolatto et al. 2003). For interferometer measurements to properly sample the full cloud structure a multi-scale analysis, such as that presented here or the more rigorous “dendrogram” approach recently described by Rosolowsky et al. (2008), is necessary.

Although our dynamical and dust-based results appear consistent with this simple picture, other recent results suggest a more complex relationship between the two measurements. Bot et al. (2009, in prep.) recently measured the relationship between sub-millimeter dust emission and CO-based dynamical masses in the southwest part of the SMC Bar. Even after controlling for

contamination by an extended superstructure of CO-free H_2 , they find that virial masses are systematically lower than dust-based H_2 masses on the scale of individual CO-bright regions. This might arise if clouds are short-lived (i.e., presently collapsing) or partially supported by magnetic fields. Alternatively it may reflect altered dust properties in dense cloud cores. The virial-dust discrepancy measured by Bot et al. and the multiscale virial-dust measurements presented here can both be readily applied to simulated clouds and multi-tracer observations of Galactic GMCs. It will be interesting to see whether these measurements can be replicated purely by altering the CO-emitting surface inside of a cloud (as it appears from our simple model) or if they constrain SMC cloud structure to be genuinely different from that in the Milky Way (as appears to be the case from the Bot et al. results).

6. SUMMARY AND DISCUSSION

We combine far infrared emission, CO line emission, and a 21-cm H I map to study the structure of CO, dust, and H_2 in the SMC star forming complex N83.

Two recent surveys of the SMC using *Spitzer* (S³MC Bolatto et al. 2007, and SAGE-SMC, Gordon et al., in prep.) allow us to estimate the distributions of dust and H_2 at high spatial resolution. We calibrate a method to derive the equilibrium dust temperature, T_{dust} , and optical depth at $160\mu\text{m}$, τ_{160} , along the line of sight using only *Spitzer* data. Applying this method and assuming that the diffuse ISM of the SMC Wing is mostly H I, we determine the dust-to-gas ratio (*DGR*) using the τ_{160} and H I maps. We find τ_{160} to be a good tracer of $N(\text{H I})$ with $\tau_{160} = 1.4_{-0.5}^{+0.8} \times 10^{-26} \text{ cm}^2 N(\text{H})$, implying a *DGR* 17_{-6}^{+10} (1σ) times lower than that in the Solar Neighborhood. High residuals about the $\tau_{160} - N(\text{H I})$ relation come almost exclusively from regions of active star formation, with the largest residuals from N83 itself. The most likely origin for these high residuals is dust associated with H_2 , though several important systematic uncertainties remain unconstrained (Appendix A). Considering several pieces of evidence (the metallicity of the N84C H II region, UV spectra of a nearby star, and the *DGR* in nearby diffuse ISM) we adopt a *DGR* of $N(\text{H})/E(B - V) \approx 5 \times 10^{22} \text{ cm}^{-2} \text{ mag}^{-1}$ ($\tau_{160} = 2.8 \times 10^{-26} \text{ cm}^2 N(\text{H})$) for N83 itself, but note this as a significant uncertainty with the plausible range spanning $N(\text{H})/E(B - V) = 3\text{--}10 \times 10^{22} \text{ cm}^{-2} \text{ mag}^{-1}$. Combining this *DGR* with τ_{160} and the measured H I distribution, we derive a map of H_2^{FIR} in N83.

Comparing CO intensity, kinematics, dust, and H_2 we find:

1. The CO-to- H_2 conversion factor averaged over the part of the N83/N84 region mapped by SEST is very high, $4\text{--}11 \times 10^{21} \text{ cm}^{-2} (\text{K km s}^{-1})^{-1}$ or $\approx 20\text{--}55$ times the Galactic value. Despite the large discrepancy from the Galactic X_{CO} , there is reasonable agreement between the distributions of CO and H_2 traced by dust: a rank correlation coefficient ≈ 0.7 relates the two over the SEST field.
2. Bright CO is more confined than H_2 , so that X_{CO} varies across the region, with the lowest (most

nearly Galactic) values near the CO peaks. The magnitude (or existence) of an extended, truly CO-free envelope is a sensitive function of the adopted *DGR*. Our best estimate is that such an envelope does exist, with $\Sigma_{\text{H}_2} \approx 100 \text{ M}_\odot \text{ pc}^{-2}$ where $I_{\text{CO}} \sim 0$.

3. CO emission is a function of line-of-sight extinction, which we estimate from τ_{160} . Bright CO emission is largely confined to regions with $A_V \gtrsim 2$ mag. This agrees well with modeling of SMC clouds by Lequeux et al. (1994) and roughly matches what is seen in the Milky Way. This result is robust to most of the systematic uncertainties that affect our determination of H_2 .
4. A simple model can reconcile dynamical masses (measured from CO) with H_2 (measured from dust). In this model, CO emission comes a surface within the cloud while dust emission traces all H_2 along the line of sight. The best-fit density profile and radius are $\rho \propto r^{-0.6}$ and $R = 70$ pc. These are not strongly constrained, but the density profile is similar to that inferred for Galactic clouds and the radius is consistent with that required to achieve $A_V \approx 1$ mag for our adopted *DGR* and a typical molecular cloud density.

These results — particularly the confinement of intense CO to regions of relatively high line-of-sight extinction — are all consistent with the selective photodissociation of CO relative to H_2 at low metallicities (e.g., Maloney & Black 1988; Rubio et al. 1993b,a; Israel 1997b; Bolatto et al. 1999). In this scenario, the distribution of CO emission is largely driven by need for dust to shield CO from dissociating radiation. The underlying distribution of H_2 , while subject to significant systematic uncertainties, appears similar to that in a Galactic GMC complex.

If the distribution of CO emission is indeed largely determined by dust shielding, then we expect that the ratio of CO emission to H_2 mass will depend sensitively on both the local *DGR* and the radiation field incident on the cloud. These effects may largely cancel in more massive spiral galaxies, yielding a CO-to- H_2 conversion factor that is fairly robust (e.g., Wolfire et al. 1993). In low-mass galaxies, which have high radiation fields and low *DGR*, they will tend to compound, producing extended envelopes of H_2 with little or no associated CO.

From recent large surveys of the Magellanic Clouds at infrared and millimeter wavelengths (e.g., Fukui et al. 1999; Mizuno et al. 2001; Meixner et al. 2006; Bolatto et al. 2007; Ott et al. 2008, Gordon et al., in prep.), it will be possible in the next few years to fill the right panel in Figure 7 with points from across the Clouds. This will allow the quantification of the radiation field (and perhaps density) as a “second parameter” in the $I_{\text{CO}}-A_V$ relation. It may also allow an improved calibration of X_{CO} as a function of both *DGR* and local radiation field, extending the pioneering work by Israel (1997b) to the scale of individual clouds.

Even with such data, it is unclear if CO emission can remain an effective tracer of H_2 on the scale of individual clouds. Tracing local variations in *DGR* and radiation

field to apply a spatially variable X_{CO} may not be possible or practical. Of course, CO is already well-known to be a flawed tracer of H_2 *within* Galactic clouds (e.g., Pineda et al. 2008) but retains significant utility for tracing H_2 on large scales. Over a sizable portion of a galaxy, variations in the radiation field and DGR may average out and allow a calibration to work at a basic level. Given that the options to trace H_2 in low-metallicity galaxies remain limited, a combination of dust and molecular line emission is likely to be the only widely available option in the near future. *Herschel* spectroscopy of the [CII] line

and *Fermi* observations of γ ray emission from the Magellanic Clouds, while both likely to illuminate the issue significantly, will only target a small sample of galaxies.

We thank the anonymous referee for a detailed and helpful critique. We thank Henrik Beuther for helpful comments on a draft of the paper and Mark Krumholz for a helpful discussion. We acknowledge the use of NASA's Astrophysics Data System Bibliographic Services.

REFERENCES

Abergel, A., Boulanger, F., Mizuno, A., & Fukui, Y. 1994, *ApJ*, 423, L59

Aguirre, J. E., Bezaire, J. J., Cheng, E. S., Cottingham, D. A., Cordone, S. S., Crawford, T. M., Fixsen, D. J., Knox, L., Meyer, S. S., Norgaard-Nielsen, H. U., Silverberg, R. F., Timbie, P., & Wilson, G. W. 2003, *ApJ*, 596, 273

André, M. K., Le Petit, F., Sonnentrucker, P., Ferlet, R., Roueff, E., Civeit, T., Désert, J.-M., Lacour, S., & Vidal-Madjar, A. 2004, *A&A*, 422, 483

Arce, H. G., & Goodman, A. A. 1999, *ApJ*, 512, L135

Arimoto, N., Sofue, Y., & Tsujimoto, T. 1996, *PASJ*, 48, 275

Bell, T. A., Roueff, E., Viti, S., & Williams, D. A. 2006, *MNRAS*, 371, 1865

Bernard, J. P., Abergel, A., Ristorcelli, I., Pajot, F., Torre, J. P., Boulanger, F., Giard, M., Lagache, G., Serra, G., Lamarre, J. M., Puget, J. L., Lepeintre, F., & Cambrésy, L. 1999, *A&A*, 347, 640

Bernard, J.-P., Reach, W. T., Paradis, D., Meixner, M., Paladini, R., Kawamura, A., Onishi, T., Vijh, U., Gordon, K., Indebetouw, R., Hora, J. L., Whitney, B., Blum, R., Meade, M., Babler, B., Churchwell, E. B., Engelbracht, C. W., For, B.-Q., Misselt, K., Leitherer, C., Cohen, M., Boulanger, F., Frogel, J. A., Fukui, Y., Gallagher, J., Gorjian, V., Harris, J., Kelly, D., Latter, W. B., Madden, S., Markwick-Kemper, C., Mizuno, A., Mizuno, N., Mould, J., Nota, A., Oey, M. S., Olsen, K., Panagia, N., Perez-Gonzalez, P., Shibai, H., Sato, S., Smith, L., Staveley-Smith, L., Tielens, A. G. G. M., Ueta, T., Van Dyk, S., Volk, K., Werner, M., & Zaritsky, D. 2008, *AJ*, 136, 919

Blitz, L., Fukui, Y., Kawamura, A., Leroy, A., Mizuno, N., & Rosolowsky, E. 2007, in *Protostars and Planets V*, ed. B. Reipurth, D. Jewitt, & K. Keil, 81–96

Bohlin, R. C., Savage, B. D., & Drake, J. F. 1978, *ApJ*, 224, 132

Bolatto, A. D., Jackson, J. M., & Ingalls, J. G. 1999, *ApJ*, 513, 275

Bolatto, A. D., Leroy, A., Israel, F. P., & Jackson, J. M. 2003, *ApJ*, 595, 167

Bolatto, A. D., Leroy, A. K., Rosolowsky, E., Walter, F., & Blitz, L. 2008, *ApJ*, 686, 948

Bolatto, A. D., Simon, J. D., Stanimirović, S., van Loon, J. T., Shah, R. Y., Venn, K., Leroy, A. K., Sandstrom, K., Jackson, J. M., Israel, F. P., Li, A., Staveley-Smith, L., Bot, C., Boulanger, F., & Rubio, M. 2007, *ApJ*, 655, 212

Boselli, A., Lequeux, J., & Gavazzi, G. 2002, *A&A*, 384, 33

Bot, C., Boulanger, F., Lagache, G., Cambrésy, L., & Egret, D. 2004, *A&A*, 423, 567

Bot, C., Boulanger, F., Rubio, M., & Rantakyro, F. 2007, *A&A*, 471, 103

Bot, C., Helou, G., Boulanger, F., Lagache, G., Miville-Deschénes, M.-A., Draine, B., & Martin, P. 2009, ArXiv e-prints

Bouchet, P., Lequeux, J., Maurice, E., Prevot, L., & Prevot-Burnichon, M. L. 1985, *A&A*, 149, 330

Boulanger, F., Abergel, A., Bernard, J.-P., Burton, W. B., Desert, F.-X., Hartmann, D., Lagache, G., & Puget, J.-L. 1996, *A&A*, 312, 256

Boulanger, F., Bronfman, L., Dame, T. M., & Thaddeus, P. 1998, *A&A*, 332, 273

Brüns, C., Kerp, J., Staveley-Smith, L., Mebold, U., Putman, M. E., Haynes, R. F., Kalberla, P. M. W., Muller, E., & Filipovic, M. D. 2005, *A&A*, 432, 45

Cambrésy, L., Boulanger, F., Lagache, G., & Stepnik, B. 2001, *A&A*, 375, 999

Cambrésy, L., Jarrett, T. H., & Beichman, C. A. 2005, *A&A*, 435, 131

Caplan, J., Ye, T., Deharveng, L., Turtle, A. J., & Kennicutt, R. C. 1996, *A&A*, 307, 403

Dale, D. A., & Helou, G. 2002, *ApJ*, 576, 159

Dame, T. M., Hartmann, D., & Thaddeus, P. 2001, *ApJ*, 547, 792

Desert, F.-X., Boulanger, F., & Puget, J. L. 1990, *A&A*, 237, 215

Dickey, J. M., Mebold, U., Marx, M., Amy, S., Haynes, R. F., & Wilson, W. 1994, *A&A*, 289, 357

Dickey, J. M., Mebold, U., Stanimirović, S., & Staveley-Smith, L. 2000, *ApJ*, 536, 756

Draine, B. T., Dale, D. A., Bendo, G., Gordon, K. D., Smith, J. D. T., Armus, L., Engelbracht, C. W., Helou, G., Kennicutt, Jr., R. C., Li, A., Roussel, H., Walter, F., Calzetti, D., Moustakas, J., Murphy, E. J., Rieke, G. H., Bot, C., Hollenbach, D. J., Sheth, K., & Teplitz, H. I. 2007, *ApJ*, 663, 866

Draine, B. T., & Lee, H. M. 1984, *ApJ*, 285, 89

Draine, B. T., & Li, A. 2007, *ApJ*, 657, 810

Dutra, C. M., Ahumada, A. V., Clariá, J. J., Bica, E., & Barbuy, B. 2003, *A&A*, 408, 287

Dwek, E. 1997, *ApJ*, 484, 779

—. 1998, *ApJ*, 501, 643

Elmegreen, B. G. 1989, *ApJ*, 338, 178

Fitzpatrick, E. L. 1984, *ApJ*, 282, 436

—. 1985, *ApJS*, 59, 77

Fukui, Y., Mizuno, N., Yamaguchi, R., Mizuno, A., Onishi, T., Ogawa, H., Yonekura, Y., Kawamura, A., Tachihara, K., Xiao, K., Yamaguchi, N., Hara, A., Hayakawa, T., Kato, S., Abe, R., Saito, H., Mano, S., Matsunaga, K., Mine, Y., Moriguchi, Y., Aoyama, H., Asayama, S.-i., Yoshikawa, N., & Rubio, M. 1999, *PASJ*, 51, 745

Galliano, F., Madden, S. C., Jones, A. P., Wilson, C. D., Bernard, J.-P., & Le Peintre, F. 2003, *A&A*, 407, 159

Gordon, K. D., Bot, C., Muller, E., Misselt, K. A., Bolatto, A., Bernard, J., Reach, W., Engelbracht, C. W., Babler, B., Bracker, S., Block, M., Clayton, G. C., Hora, J., Indebetouw, R., Israel, F. P., Li, A., Madden, S., Meade, M., Meixner, M., Sewilo, M., Shiao, B., Smith, L. J., van Loon, J. T., & Whitney, B. A. 2008a, ArXiv e-prints

Gordon, K. D., Clayton, G. C., Misselt, K. A., Landolt, A. U., & Wolff, M. J. 2003, *ApJ*, 594, 279

Gordon, K. D., Engelbracht, C. W., Rieke, G. H., Misselt, K. A., Smith, J.-D. T., & Kennicutt, Jr., R. C. 2008b, *ApJ*, 682, 336

Heyer, M., Krawczyk, C., Duval, J., & Jackson, J. M. 2008, ArXiv e-prints

Israel, F. 2000, in *Molecular Hydrogen in Space*, ed. F. Combes & G. Pineau Des Forets, 293–+

Israel, F. P. 1988, in *Astrophysics and Space Science Library*, Vol. 147, *Millimetre and Submillimetre Astronomy*, ed. R. D. Wolstencroft & W. B. Burton, 281–305

Israel, F. P. 1997a, *A&A*, 317, 65

—. 1997b, *A&A*, 328, 471

Israel, F. P., de Graauw, T., van de Stadt, H., & de Vries, C. P. 1986, *ApJ*, 303, 186

Israel, F. P., Johansson, L. E. B., Lequeux, J., Booth, R. S., Nyman, L. A., Crane, P., Rubio, M., de Graauw, T., Kutner, M. L., Gredel, R., Boulanger, F., Garay, G., & Westerlund, B. 1993, *A&A*, 276, 25

Israel, F. P., Johansson, L. E. B., Rubio, M., Garay, G., de Graauw, T., Booth, R. S., Boulanger, F., Kutner, M. L., Lequeux, J., & Nyman, L.-A. 2003, A&A, 406, 817

Issa, M. R., MacLaren, I., & Wolfendale, A. W. 1990, A&A, 236, 237

Krumholz, M. R., McKee, C. F., & Tumlinson, J. 2009, ApJ, 693, 216

Larson, R. B. 1981, MNRAS, 194, 809

Laureijs, R. J., Clark, F. O., & Prusti, T. 1991, ApJ, 372, 185

Lee, H., Skillman, E. D., Cannon, J. M., Jackson, D. C., Gehrz, R. D., Polomski, E. F., & Woodward, C. E. 2006, ApJ, 647, 970

Lequeux, J., Le Bourlot, J., Des Forets, G. P., Roueff, E., Boulanger, F., & Rubio, M. 1994, A&A, 292, 371

Leroy, A., Bolatto, A., Stanimirović, S., Mizuno, N., Israel, F., & Bot, C. 2007, ApJ, 658, 1027

Leroy, A., Bolatto, A., Walter, F., & Blitz, L. 2006, ApJ, 643, 825

Lisenfeld, U., & Ferrara, A. 1998, ApJ, 496, 145

Lombardi, M., Alves, J., & Lada, C. J. 2006, A&A, 454, 781

Madden, S. C., Galliano, F., Jones, A. P., & Sauvage, M. 2006, A&A, 446, 877

Madden, S. C., Poglitsch, A., Geis, N., Stacey, G. J., & Townes, C. H. 1997, ApJ, 483, 200

Maloney, P., & Black, J. H. 1988, ApJ, 325, 389

McKee, C. F. 1989, ApJ, 345, 782

Meixner, M., Gordon, K. D., Indebetouw, R., Hora, J. L., Whitney, B., Blum, R., Reach, W., Bernard, J.-P., Meade, M., Babler, B., Engelbracht, C. W., For, B.-Q., Misselt, K., Vijh, U., Leitherer, C., Cohen, M., Churchwell, E. B., Boulanger, F., Frogel, J. A., Fukui, Y., Gallagher, J., Gorjian, V., Harris, J., Kelly, D., Kawamura, A., Kim, S., Latter, W. B., Madden, S., Markwick-Kemper, C., Mizuno, A., Mizuno, N., Mould, J., Nota, A., Oey, M. S., Olsen, K., Onishi, T., Paladini, R., Panagia, N., Perez-Gonzalez, P., Shibai, H., Sato, S., Smith, L., Staveley-Smith, L., Tielens, A. G. G. M., Ueta, T., Dyk, S. V., Volk, K., Werner, M., & Zaritsky, D. 2006, AJ, 132, 2268

Miville-Deschénes, M.-A., & Lagache, G. 2005, ApJS, 157, 302

Mizuno, N., Rubio, M., Mizuno, A., Yamaguchi, R., Onishi, T., & Fukui, Y. 2001, PASJ, 53, L45

Ossenkopf, V., & Henning, T. 1994, A&A, 291, 943

Ott, J., Wong, T., Pineda, J. L., Hughes, A., Muller, E., Li, Z.-Y., Wang, M., Staveley-Smith, L., Fukui, Y., Weiß, A., Henkel, C., & Klein, U. 2008, Publications of the Astronomical Society of Australia, 25, 129

Pak, S., Jaffe, D. T., van Dishoeck, E. F., Johansson, L. E. B., & Booth, R. S. 1998, ApJ, 498, 735

Papadopoulos, P. P., Thi, W.-F., & Viti, S. 2002, ApJ, 579, 270

Pelupessy, F. I., Papadopoulos, P. P., & van der Werf, P. 2006, ApJ, 645, 1024

Pineda, J. E., Caselli, P., & Goodman, A. A. 2008, ApJ, 679, 481

Rosolowsky, E., Engargiola, G., Plambeck, R., & Blitz, L. 2003, ApJ, 599, 258

Rosolowsky, E., & Leroy, A. 2006, PASP, 118, 590

Rosolowsky, E. W., Pineda, J. E., Kauffmann, J., & Goodman, A. A. 2008, ApJ, 679, 1338

Rubio, M., Boulanger, F., Rantakyro, F., & Contursi, A. 2004, A&A, 425, L1

Rubio, M., Garay, G., Montani, J., & Thaddeus, P. 1991, ApJ, 368, 173

Rubio, M., Lequeux, J., & Boulanger, F. 1993a, A&A, 271, 9

Rubio, M., Lequeux, J., Boulanger, F., Booth, R. S., Garay, G., de Graauw, T., Israel, F. P., Johansson, L. E. B., Kutner, M. L., & Nyman, L. A. 1993b, A&A, 271, 1

Russell, S. C., & Dopita, M. A. 1990, ApJS, 74, 93

Schnee, S., Bethell, T., & Goodman, A. 2006, ApJ, 640, L47

Schnee, S., Li, J., Goodman, A. A., & Sargent, A. I. 2008, ApJ, 684, 1228

Schnee, S. L., Ridge, N. A., Goodman, A. A., & Li, J. G. 2005, ApJ, 634, 442

Solomon, P. M., Rivolo, A. R., Barrett, J., & Yahil, A. 1987, ApJ, 319, 730

Stanimirović, S., Staveley-Smith, L., Dickey, J. M., Sault, R. J., & Snowden, S. L. 1999, MNRAS, 302, 417

Stepnik, B., Abergel, A., Bernard, J.-P., Boulanger, F., Cambrésy, L., Giard, M., Jones, A. P., Lagache, G., Lamarre, J.-M., Meny, C., Pajot, F., Le Peintre, F., Ristorcelli, I., Serra, G., & Torre, J.-P. 2003, A&A, 398, 551

Strong, A. W., & Mattox, J. R. 1996, A&A, 308, L21

Thronson, Jr., H. A. 1988, in NATO ASIC Proc. 232: Galactic and Extragalactic Star Formation, ed. R. E. Pudritz & M. Fich, 621–+

Thronson, Jr., H. A., Greenhouse, M., Hunter, D. A., Telesco, C. M., & Harper, D. A. 1988, ApJ, 334, 605

Thronson, Jr., H. A., Walker, C. K., Walker, C. E., & Maloney, P. 1987, ApJ, 318, 645

Tumlinson, J., Shull, J. M., Rachford, B. L., Browning, M. K., Snow, T. P., Fullerton, A. W., Jenkins, E. B., Savage, B. D., Crowther, P. A., Moos, H. W., Sembach, K. R., Sonneborn, G., & York, D. G. 2002, ApJ, 566, 857

Walter, F., Cannon, J. M., Roussel, H., Bendo, G. J., Calzetti, D., Dale, D. A., Draine, B. T., Helou, G., Kennicutt, Jr., R. C., Moustakas, J., Rieke, G. H., Armus, L., Engelbracht, C. W., Gordon, K., Hollenbach, D. J., Lee, J., Li, A., Meyer, M. J., Murphy, E. J., Regan, M. W., Smith, J.-D. T., Brinks, E., de Blok, W. J. G., Bigiel, F., & Thornley, M. D. 2007, ApJ, 661, 102

Walter, F., Taylor, C. L., Hüttemeister, S., Scoville, N., & McIntyre, V. 2001, AJ, 121, 727

Walter, F., Weiss, A., Martin, C., & Scoville, N. 2002, AJ, 123, 225

Wilke, K., Klaas, U., Lemke, D., Mattila, K., Stickel, M., & Haas, M. 2004, A&A, 414, 69

Wilson, B. A., Dame, T. M., Masheder, M. R. W., & Thaddeus, P. 2005, A&A, 430, 523

Wilson, C. D. 1995, ApJ, 448, L97+

Wilson, C. D., Scoville, N., Madore, B. F., Sanders, D. B., & Freedman, W. L. 1988, ApJ, 333, 611

Wolfire, M. G., Hollenbach, D., & Tielens, A. G. G. M. 1993, ApJ, 402, 195

APPENDIX

SYSTEMATIC UNCERTAINTIES IN $N(\text{H}_2^{\text{FIR}})$

Several systematic uncertainties may affect $N(\text{H}_2^{\text{FIR}})$ but are hard to quantify and so not reflected in our Monte Carlo estimate of the uncertainties. Here we discuss these for the specific case of N83 (for a more general discussion see Israel 1997a). We find no strong reason to doubt that Equation 7 yields an approximate estimate of $N(\text{H}_2)$. N83 appears unlikely to harbor a significant population of cold dust and we do not observe compelling evidence that dust traces mostly warm ionized gas or high optical depth H I. There is likely some blending of populations along the line of sight, but the magnitude of the effect is unclear. Grain processing is largely unconstrained, but we note the dissimilarity between N83 and the dense, cold cores where these effects are usually discussed.

Blending of Populations Along the Line of Sight: N83 is a dense, active region and the line-of-sight distance through the SMC may be very long. As a result, the observed dust emission may represent a blend of several dust populations with different temperatures. The likely effect is that we overestimate the average T_{dust} along the line of sight and therefore underestimate τ_{160} and H_2^{FIR} (e.g., see tests on simulated clouds by Schnee et al. 2006).

Cold Dust: A related concern is that our longest wavelength data are at $160\mu\text{m}$. As a result, we would miss any population of cold dust. In the Milky Way, when cold, molecular filaments can be isolated from embedded star

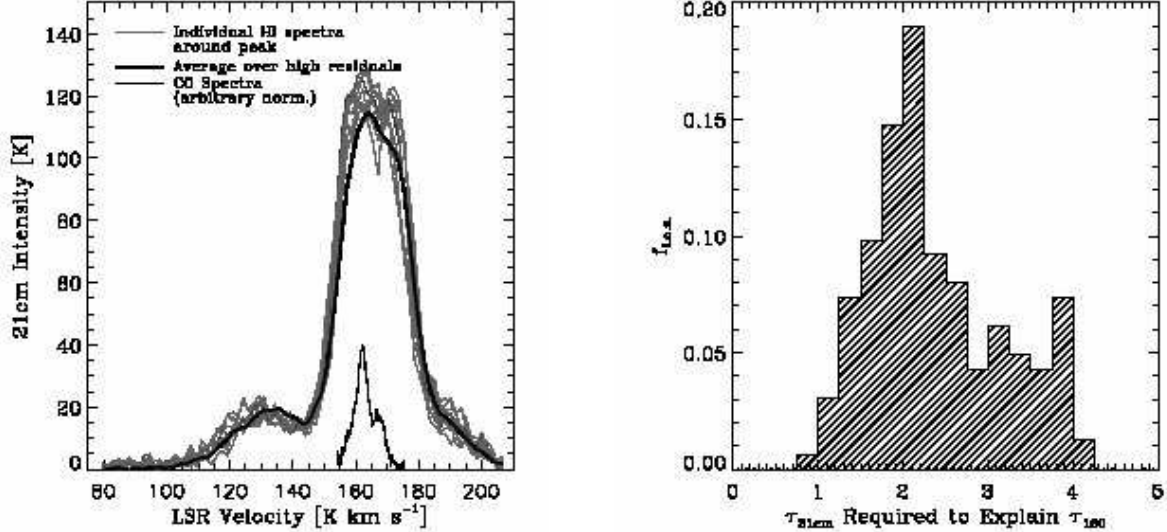


FIG. 9.— (left) The average H I spectrum over the region of high residuals (black) and spectra from individual lines of sight in this area (gray). The spectrum of CO emission (with an arbitrary normalization) is shown below the H I. (right) The distribution of opacities in the (integrated) 21cm line required to explain the residuals in highest contour in Figure 4. Although individual spectra show some evidence of optical thickness, we see no clear signature of self absorption. The line-integrated values of $\tau_{21\text{cm}}$ required to explain τ_{160} in N83 are mostly higher than the peak values of $\tau_{21\text{cm}}$ measured anywhere in the SMC by Dickey et al. (2000).

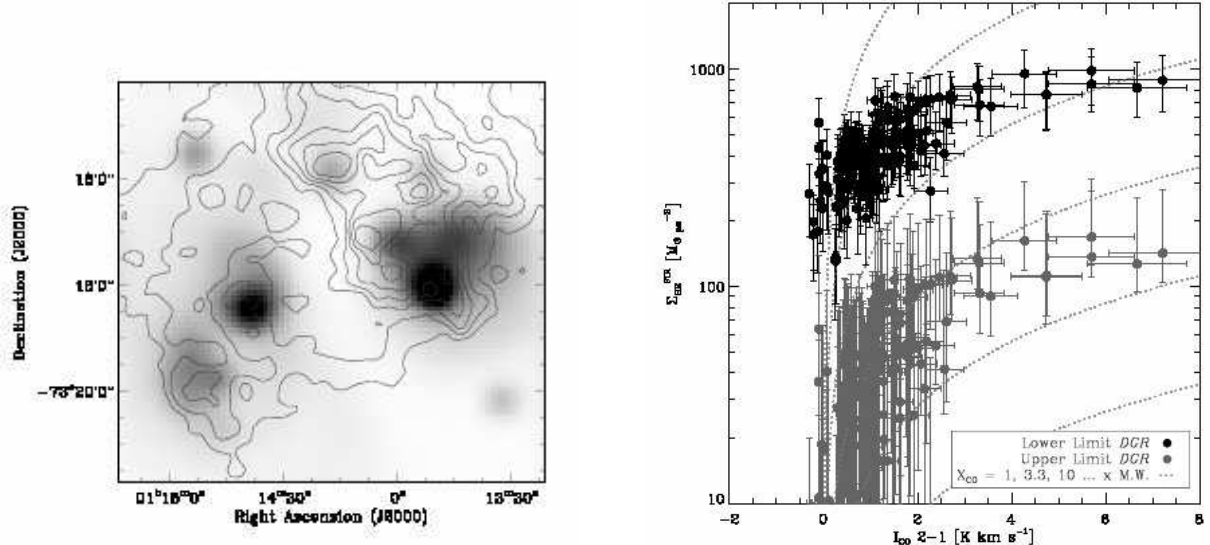


FIG. 10.— (left) H α emission (gray scale) with $\Sigma_{\text{H}_2}^{\text{FIR}}$ shown in contour (both at 36'' resolution). Although H α and H_2^{FIR} roughly coincide on large scales (Figure 4), the detailed distributions are not a good match. (right) The effect of changing DGR to the most extreme plausible values on the relationship between $\Sigma_{\text{H}_2}^{\text{FIR}}$ (y-axis) and I_{CO} (x-axis, only $J = 2 \rightarrow 1$ shown). The black points show the lowest plausible DGR in N83, that found in the nearby diffuse gas. The gray points show the highest plausible DGR, ~ 3 times this value.

formation, they are often observed to have low dust temperatures ($T \lesssim 15$ K) and little out-of-equilibrium emission (e.g., Laureijs et al. 1991; Bernard et al. 1999; Stepnik et al. 2003). As with blending of several populations, cold dust is most likely to be associated with the dense, molecular environment of N83. Missing cold dust would lead us to underestimate τ_{160} and $N(\text{H}_2^{\text{FIR}})$.

Given the high T_{dust} in N83 and the presence of ongoing, vigorous star formation we consider it unlikely that there is a significant amount of cold dust present. We attempt a simple test that reveals the presence of cold filaments in Galactic GMCs (Abergel et al. 1994; Boulanger et al. 1998): we take the median I_{160}/I_{70} over the region, scale the 70 μm map by this value, and subtract it from the 160 μm map. This should reveal the location of any local 160 μm excess, a likely signature of cold dust. We find no such excess associated with N83 as a whole or the CO peaks in particular.

Other Gas Phases: We refer to the results of Equation 7 as "H $^{\text{FIR}}$ " but this is actually an estimate of all gas not traced by the 21-cm transition. Some of this might be high optical depth H I or warm ionized gas. Neither appears to

be a plausible explanation for the majority of such gas in N83. This agrees with results from the Milky Way, where excess dust emission identified in a similar way also appears to correspond mostly to H₂ (Dame et al. 2001).

The right panel in Figure 9 shows the H I opacities required to account for τ_{160} in N83 given our adopted *DGR*. These values, $\tau_{21\text{cm}} = 2\text{--}4$, are higher than those implied by the fit of Dickey et al. (2000), which yields a maximum line-integrated $\tau_{21\text{cm}} \sim 0.55$ (correction factor ~ 1.3) near N83. Indeed, most of the line-integrated values of $\tau_{21\text{cm}}$ in Figure 9 are higher than any of the *peak* $\tau_{21\text{cm}}$ values (i.e., $\tau_{21\text{cm}}$ in the most opaque velocity channel) measured by Dickey et al. (2000) in the SMC (maximum ~ 1.7). though that study did not probe any star-forming peaks; toward the starburst region 30 Doradus in the LMC Dickey et al. (1994) found peak $\tau_{21\text{cm}}$ values of ~ 2 , which is still too small to achieve the line-integrated value of $\tau_{21\text{cm}}$ required account for τ_{160} in N83. The 21cm spectra do show some evidence of optical thickness at a brightness temperature of ~ 120 K, but no clear signs of self-absorption at the velocity of the CO peak (left panel in Figure 9). We cannot rule out unlucky geometry, but achieving line-integrated optical depths of 2–4 without invoking a contrived scenario appears difficult.

Warm ionized gas also seems unlikely to account for most of H₂^{FIR}. The left panel in Figure 10 shows contours of $\Sigma_{\text{H}_2}^{\text{FIR}}$ over an H α image (at matched resolution) in the SEST field. Although high τ_{160} residuals correspond to H α emission on large scales, the detailed distribution is not a particularly good match. The rank correlation coefficient between H α and H₂^{FIR} over the area observed by SEST is ~ 0.1 , much lower than the 0.7 relating H₂^{FIR} and CO. H α emission is proportional to $\int n^2 dl$ and so obviously a flawed tracer of the true warm gas column ($\int ndl$), but the poor correspondence on small scales still argues that most H₂^{FIR} is not actually warm ionized gas.

Dust Processing in Molecular Clouds: A significant but hard-to-constrain uncertainty in Equation 7 is if and how dust properties vary between N83 and the surrounding ISM. The most likely variations are increases in the FIR emissivity or the *DGR*. In the Milky Way, the FIR emissivity of dust (τ_{FIR}/A_V) does appear to increase towards dense regions, increasing by $\sim 30\text{--}50\%$ above $A_V \sim 1$ mag (e.g., Arce & Goodman 1999; Dutra et al. 2003; Cambrésy et al. 2005). Cambrésy et al. (2001), Stepnik et al. (2003), and Cambrésy et al. (2005) argue that this is due to the creation of fluffy dust grains with low albedos (Dwek 1997) via grain-grain coagulation or accretion of gas. At the same time, build-up of existing grains in molecular clouds and dust creation in Type II supernovae or stellar winds (e.g., Dwek 1998) may cause the *DGR* ratio near star-forming regions to be higher than in the surrounding ISM.

The magnitude of grain growth in GMCs remains very poorly constrained and in an active environment like N83 it will be balanced against grain destruction (e.g., in shocks). Further, the high dust temperatures, low integrated extinctions ($A_V \lesssim 2$ mag almost everywhere), and weak CO emission in N83 are a far cry from the high density, high extinction environments in which grain coagulation or the formation of icy mantles are usually modeled or observed (e.g., Ossenkopf & Henning 1994). Moreover, as pointed out by Bernard et al. (2008), increased emissivity in Milky Way clouds is often associated with diminished small grain emission (e.g., Schnee et al. 2008), while N83 exhibits increased I_{70}/I_{160} compared to its surroundings.

Because it is unclear what, if any, grain processing is at work in N83, we make no correction to the emissivity. If dust in N83 indeed has a high emissivity compared to the diffuse ISM, we will derive values of both $N(\text{H}_2^{\text{FIR}})$ and A_V that are too high. Note that our adopted *DGR* is already twice that in the surrounding diffuse gas. Increasing or decreasing the adopted *DGR* will not affect τ_{160} or A_V , but will lower or raise $N(\text{H}_2^{\text{FIR}})$.

Effect of Changing DGR on the CO-H₂ relation: The exact value of the *DGR* in N83 is the largest systematic uncertainty in our analysis. We discuss the constraints on this quantity in §4.3. In the right panel of Figure 10, we illustrate the relationship between H₂ and *DGR* in the limiting cases: *DGR* equal to that in the diffuse ISM of the SMC Wing (black) and *DGR* equal to three times this value (gray).

There are two main conclusions to draw from this comparison. First, the existence and magnitude of a truly CO-free H₂ envelope (the *y*-intercept of the points) depends sensitively on the adopted *DGR*; the lowest plausible value is (partially by construction) consistent with no envelope and the highest value implies an envelope with surface densities $\sim 200\text{--}400 \text{ M}_\odot \text{ pc}^{-2}$, 1–2 times the average surface density of a Galactic GMC. Second, the average CO-to-H₂ conversion factor varies between 10 and 100 times Galactic over the full range of possible *DGR*. The qualitative behavior (meaning the presence of bright I_{CO} only above a certain Σ_{H_2} threshold) remains the same. We emphasize that the relationship between A_V (or τ_{160}) and I_{CO} is unaffected by the choice of *DGR*.